Snookie

An Autonomous Underwater Vehicle with Artificial Lateral-Line System

Andreas N. Vollmayr and Stefan Sosnowski and Sebastian Urban and
Sandra Hirche and J. Leo van Hemmen

Abstract In this work we present Snookie, an autonomous underwater vehicle with an artificial lateral-line system. Integration of the artificial lateral-line system with other sensory modalities is to enable the robot to perform behaviours as observed in fish, such as obstacle detection and geometrical-shape reconstruction by means of hydrodynamic images. The present paper consists of three sections devoted to design of the robot, its lateral-line system, and processing of the ensuing flow-sensory data. The artificial lateral-line system of *Snookie* is presented in detail, together with a simple version of a flow reconstruction algorithm applicable to both the artificial lateral-line system and, e.g., the blind Mexican cave fish. More in particular, the first section deals with the development of the autonomous underwater vehicle *Snookie*, which provides the functionality and is tailored to the requirements of the artificial lateral-line system. The second section is devoted to the implementation of the artificial lateral-line system that consists of an array of hot thermistor anemometers to be integrated in the nozzle. In the final sec-

---

Andreas N. Vollmayr

Lehrstuhl für theoretische Biophysik, Physik Department T35, TU München, James-Franck-Straße, 85748 Garching, e-mail: `andreas.vollmayr@tum.de`

Stefan Sosnowski

Lehrstuhl für Informationstechnische Regelung, Fakultät für Elektro- und Informationstechnik, TU München, Barer Straße 21, 80333 München, e-mail: `sosnowski@tum.de`

Sebastian Urban

Lehrstuhl für theoretische Biophysik, Physik Department T35, TU München, James-Franck-Straße, 85748 Garching, e-mail: `sebastian.urban@tum.de`

Sandra Hirche

Lehrstuhl für Informationstechnische Regelung, Fakultät für Elektro- und Informationstechnik, TU München, Barer Straße 21, 80333 München, e-mail: `hirche@tum.de`

J. Leo van Hemmen

Lehrstuhl für theoretische Biophysik, Physik Department T35, TU München, James-Franck-Straße, 85748 Garching, e-mail: `lvh@tum.de`

tion the information processing ensuing from the flow sensors and leading
to conclusions about the environment is presented. The measurement of the
tangential velocities at the artificial lateral-line system together with the no-
penetration condition provides the robot with Cauchy boundary conditions
so that the hydrodynamic mapping of potential flow onto the lateral line can
be inverted. Through this inversion information is accessible from the flow
around the artificial lateral line about objects in the neighbourhood, which
alter the flow field.

Key words: Artificial lateral-line system, autonomous underwater robot,
blind Mexican cave fish, flow-field reconstruction, flow sensing, highly ma-
noeuvrable AUV, hot thermistor velocimetry, hydrodynamic image, subma-
rine dynamics

1 Introduction

Even if completely blind fish are able to locate obstacles and avoid them
under poor visual conditions (Dijkgraaf, 1933, 1963). Studies on the blind
cave form of *Astyanax mexicanus* and the closely related *Astyanax jordani*
(previously known as *Anoptichthys jordani*) show that these fish are able to
detect and also discriminate objects, if gliding past or towards them at close
distance. The objects are perceived by means of the lateral-line organ, which
is distributed along the body of the fish and responds to the movement of the
water relative to the fish's skin (Van Trump and McHenry, 2008; Mogdans
and Bleckmann, 2012). The presence of objects leads to an alteration of the
flow field around the fish, which creates a "hydrodynamic image" (Hassan,
1989) of the surroundings on the fish's body.

On the basis of behavioural experiments some of the tasks the lateral sys-
tem is involved in and some of the features of stimuli that are reconstructed by
the lateral-line system have been identified. For most objects moving towards
the lateral-line system at some distances the flow field may be approximated
by that of a dipole – a moving sphere of equal volume (Howe, 2006, pp. 24) –
since higher multipoles decrease much more rapidly with increasing distance
to the moving object. It has been shown that goldfish and mottled sculpin
are able to determine the position of the dipole (Coombs, 1994). Mottled
sculpins respond to the presentation of an oscillating sphere as lowest-order
representation of the flow field of prey with hunting behaviour and a strike
towards the dipole source (Coombs and Conley, 1997a; Conley and Coombs,
1998; Coombs et al, 2001; Coombs and Patton, 2009). Experiments carried
out on goldfish (Vogel and Bleckmann, 2001) suggest that fish are in principle
also able to distinguish the direction of motion, speed, shape and size of solid
objects. As a natural example schooling can be done solely by perception of
the flow fields of neighbouring fish (Partridge and Pitcher, 1980).

The blind cave form of *Astyanax mexicanus* can detect, avoid, and also discriminate objects, when gliding past or towards them at close distance (Teyke, 1985; Hassan, 1986; Windsor et al, 2008). For the blind Mexican cave fish, on the basis of behavioural experiments (von Campenhausen et al, 1981; Weissert and von Campenhausen, 1981; Hassan, 1986), there is no doubt about its elaborate capabilities sensing its environment by means of the lateral-line system. Although it is not quite clear what the capabilities of a lateral-line system really are and what tasks it can be used for, the example of the blind Mexican cave fish shows that it is obviously possible to make vital decisions based solely on information mediated by the surrounding fluid motion.

Flow sensing is usually split up in either the reception of a vortex structure or the reception of irrotational flow. Major objects moving in water produce a wake provided that they are not streamlined. In a large range of Reynolds numbers, the wake releases vortex structures, which are called von Kármán vortex street. Especially the strokes of the tail fin of fish leave behind prominent flow structures. These vortex structures mark the trace of swimming fish for quite a while (Hanke et al, 2000; Hanke, 2004). Because of the low viscosity and the high mass of water, vortices are quite stable and may remain up to several minutes. Catfish have been shown to sense the vortex street with the lateral-line system during prey capture (Pohlmann et al, 2001, 2004). Wake tracking can in principle also be done by other flow sensory systems such as the whiskers of harbour seals (Dehnhardt et al, 2001; Wieskotten et al, 2011). While the mapping of a vortex on the fish's lateral-line system is understood quite well (Franosch et al, 2009), it is a non-trivial task to determine the properties of the vortex-producing object (Akanyeti et al, 2011).

The flow field of these vortex structures – seen from the perspective of extracting information – is completely different from the flow field, e.g., the blind Mexican cave fish produces (Handelsman and Keller, 1967; Geer, 1975; Hassan, 1985, 1992a,b, 1993) to sense its environment. The flow field in front of and besides the blind Mexican cave fish may be treated irrotational as long it is moving through nearly undisturbed water. The vorticity produced by the action of viscosity at the surface of the fish is convected to the rear with the incident flow. This is usually expressed by a high Reynolds number in front of the fish resulting in a inviscid and irrotational region of flow around the snout well described by a velocity potential Φ for the incompressible Euler equations (Panton, 2005; Oertel and Mayes, 2004). Of course, the frequencies and the velocities involved in the problem guarantee incompressibility at every time.

Any object in the near surrounding disturbs the flow field on the surface of the fish compared to open water, the *hydrodynamic image*. The properties of a hydrodynamic image of a moving body mapped through an incompressible inviscid irrotational fluid are discussed in (Sichert et al, 2009) by performing a multipole expansion of the flow field of varying shapes. The flow field is measured by a transparent artificial lateral line, meaning that the presence of the artificial lateral line does not disturb the flow field of the moving body.

Then from the estimated multipole moments basic information about the shape of the moving body is extracted, e.g., the volume is represented by the dipole moment. The conclusions are that – given a realistic resolution of the lateral-line sensors – the upper bounds for the range of localisation and shape reconstruction are roughly the size of the lateral-line system and the size of the moving object. The hydrodynamic image therefore only provides information about the environment in a very close range.

The present project of *Snookie* aims at the integration of an artificial lateral-line system (ALL) to a technical system, more specifically an underwater robot. Transferring the mentioned capabilities of the lateral-line organ to a robotic system would be beneficial in a number of ways. It complements existing established sensor technology. For instance, sonar sensors have a minimum distance at which to measure, with a blind zone within that distance, whereas camera- or laser-based systems are dependent on visual conditions. Its function is passive in the sense that it uses information that is present anyway due to the physics of bodies moving in water. The motion control of a group of several platforms equipped with flow sensory systems is possible without sensor interference or the need for data exchange. Also reflections, like with sonar systems in narrow spaces, do not interfere with the measurement. Moreover, the mapping of the hydrodynamic properties of the environment is enabled. As will turn out in the course of this work, reconstruction of the environment is doable with little computational effort. An explicit mathematical description of the underlying algorithms is presented.

From the constraints of the hydrodynamic image severe requirements follow for the implementation of an ALL on a moving robot. The lateral-line sensors must be capable of detecting small, slowly varying (Bleckmann et al, 1991) changes in the comparably strong flow field around the moving robot. The information processing must be very fast to enable the robot to react on detected changes of the immediate environment and the robot must be highly manoeuvrable in order to change the state of motion appropriately within this narrow range.

2 Related Work

Research on ALLs, the processing of the sensory data and the transfer to technical systems is not a completely new idea, but faces some inherent challenges, which are still to be solved. The biomimetic process covered in this work can be separated into three different stages: the development of an ALL (Sec. 4) the design of a robot for it (Sec. 3) and the process of acquiring information about the environment for the robot (Sec. 5). Each stage has been subject to previous or parallel research on the topic, which will be related to the proposed approaches in the following. The first stage is to build a sensory system that can mimic the function of the lateral-line system.

The basic functionality and morphology of the lateral-line system is well known (Coombs and van Netten, 2005; Bleckmann, 2008; Bleckmann and Zelick, 2009). However, the exact transfer from the hydrodynamic stimulus to the excitation of the sensor (Coombs et al, 1996; Curcić-Blake and van Netten, 2005; van Netten, 2006; Goulet et al, 2008; McHenry et al, 2008), the resulting neuronal signals (Coombs and Conley, 1997b; Engelmann et al, 2002; Chagnaud et al, 2006), and their processing is still under investigation (Kröther et al, 2002; Plachta, 2003; Engelmann and Bleckmann, 2004; Bleckmann, 2008; Künzel et al, 2011; Meyer et al, 2012).

This means that so far attempts to rebuild the lateral-line system can only lead to an approximation or abstraction of the biological counterpart. For air, building biomimetic flow sensors is significantly simpler due to the properties of the medium, especially the viscosity and conductivity. Research in biomimetic flow sensing is driven by the upcoming interest in insect-like microflight. A review on different technologies in this sector is given by Motamed and Yan (Motamed and Yan, 2005) highlighting sensor design and experiments. The focus is on the determination of forces acting on the microrobot as a feedback for control. One step further in terms of object/stimulus localisation are projects utilising arrays of biomimetic hair cells (*cilia*) as sensors. Work by Izadi et al (2010) and Dagamseh et al (2013) shows the localisation of a dipole source – a vibrating sphere – in air by measuring the deflection of artificial hair sensors. The deflection of the hair induces a capacitive change in the hair base of the sensor, which can be related to the flow velocity. Other artificial cilia are based on the piezoelectric effect, for example with polyvinylidene fluoride fibers (PVDF) (Li et al, 2010). The sensors are either used as surface neuromasts (Liu, 2007; Hsieh et al, 2011; Qualtieri et al, 2011), or integrated in a canal (Yang et al, 2011; Klein and Bleckmann, 2011; Klein et al, 2011, 2013). Both approaches can in principle be used for dipole localisation (Nguyen et al, 2011; Yang et al, 2011). An extension of the cilia approach is encapsulating them with a hydrogel cupula (Peleshanko et al, 2007). While biomimetic cilia might come close to the biological source of inspiration, the robustness, manufacturing complexity and signal-to-noise ratio are still challenges that prevent the application in an autonomous underwater vehicle.

A different approach for underwater sensing is to use thermal transport as a means for detecting the flow velocity. Hot-wire anemometers have been used for measuring flow velocities in gases and fluids (Middlebrook and Piret, 1950) for a long time, but advances in the miniaturisation make them applicable to ALLs. First trial runs were done by Coombs et al (1989), as a means of "measuring water motions used in stimulating the mechanosensory lateral-line system of a teleost fish". Micromachined arrays of hot-wire elements show the ability of localising dipole sources as good as biomimetic cilia (Chen et al, 2006; Yang et al, 2006; Pandya et al, 2007; Yang et al, 2010).

Only recently, there have been some works on the integration of ALLs or comparable sensors on underwater robots. A general overview on the state

of underwater robotics is given by Kinsey et. al. (Kinsey et al, 2006) and Nicholson (Nicholson and Healey, 2008). Hsieh et. al. describe the implementation of PVDF sensors on a robotic fish, in which the robot is supposed to sense pressure deviations due to the presence of a wall (Hsieh et al, 2011). The modelling of the wall presence is done with an image charge method that is similar to the method proposed in (Sosnowski et al, 2010). Fernandez et al place a pressure sensor array along a submarine dummy (Fernandez et al, 2007, 2009, 2011). Using principal component analysis, two different cross section shapes (round and square) can be classified if the object is moved along the dummy.

Classification of a sensor reading proofs the usability of a sensory concept. For the usage of an ALL in an a priori unknown environment a minimal number of assumption about the environment is desirable to process the sensory data. A much more general method is required, to extract shape and location of unknown objects.

Studies focused on the Mexican cave fish usually only consider the forward problem, modelling the stimulus that occurs from the hydrodynamic interference with objects on the fish's body (Hassan, 1985, 1992a,b, 1993; Windsor et al, 2010a,b). To utilise data gathered from the sensors on the robot and to obtain information about the environment the inverse problem has to be solved. Attempts to reconstruct the environment from the hydrodynamic image so far are limited to special cases with strong assumptions or prior knowledge about the environment.

The previously mentioned estimation of multipole moments of a 3-dimensional (3D) moving body requires exactly one body moving though an unbounded inviscid incompressible fluid initially at rest. The flow velocities are measured by a transparent – or more accurately, virtual – flow sensory system, which may not disturb the flow field of the moving body by its presence. Position and multipole moments up to order three are estimated simultaneously by means of a maximum-likelihood estimator given the flow velocities measured by the virtual lateral-line system. The generalisation to further incorporate an estimate of the velocity of the moving object is straightforward. The moving object may move in an arbitrary fashion.

A similar analysis has been carried out by Bouffanais et. al. (Bouffanais et al, 2010) for the 2-dimensional (2D) pressure field of the stationary potential of one body. The pressure is successively approximated by substitution of the leading terms of a Laurent series for the complex velocity potential in the stationary Bernoulli equation. This allows to discuss the dependence of pressure on distance and shape of the moving object. As an advantage, the method provides an estimate of the position and orientation of the object independent of its shape.

Quite often, the shape of one object – usually a sphere – moving relative to the physical present flow sensory system is assumed to be known. The position of the dipole can then be extracted easily from its hydrodynamic image (Coombs and van Netten, 2005; Curcić-Blake and van Netten, 2006;

Franosch et al, 2005; Pandya et al, 2006; Goulet et al, 2008). In Sec. 5 a more general method is presented that can deal with arbitrary solid stationary boundaries. The method is applicable to quasi-2D incompressible, inviscid and irrotational flow around the lateral-line system.

3 The Autonomous Underwater Vehicle *Snookie*

The submarine *Snookie* is an autonomous underwater vehicle (AUV) specifically designed as a test bed for the ALL. In this section, the concept of the robot is presented and a brief overview of its structure is given.

Special care has to be taken of the dynamics due the limited range of view of the lateral-line system. The robot must be capable of precise motion in the close vicinity of other objects at a distance of typically the diameter of the snout. Therefore, high manoeuvring capabilities are crucial. It must also be able to react on the sudden appearance of other objects in the range of view. A careful design of the hull, the fins, and the thruster arrangement, driven by an accurate physical model of its dynamics is required, which also serves the tuning of the controllers of motion.

One of the most important design considerations concerns the shape of the robot. Not only must the components of the robot fit inside, but the outline has direct influence on the functionality of the ALL. The expected sensing quality is dependent on the hydrodynamic properties of the shape of the robot, which determine the properties of the flow field of the surrounding fluid. A good compromise between ease of realisation, a simple mathematical treatise, and the quality of the hydrodynamic image is a cylindrical shape with hemispheres as caps on both ends.

The sensors of the ALL are intended to be placed in a cross in allocated mountings in the front sphere. They extend 2-3 mm above the surface to avoid boundary layer effect introduced by the surface of the hull. The spherical shape of the sensory system allows to perform approximative analytic calculations – see Sec. 5.

3.1 The Robot

The robot consists of a cylindrical watertight main compartment, in which all of the electronics is encapsulated, two half-spheres at the end of the cylinder and six thrusters. It has a total length of $L = 74$ cm and a diameter of $2R = 25$ cm. The overall mass is 32.234 kg including the flooded bow and stern, which can be fine tuned to match the water displacement of the robot for neutral buoyancy.
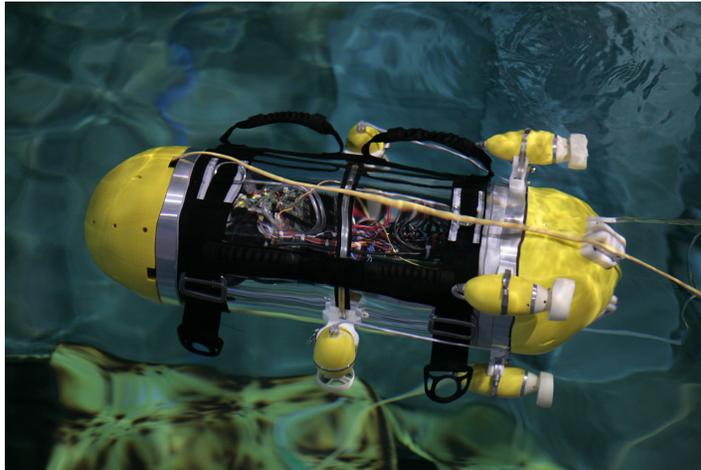
Fig. 1: *Snookie*, an autonomous underwater vehicle with an artificial lateral-line system.

To achieve high manoeuvrability, a helicopter-like multi-propeller propulsion system is adapted from the AMOUR V robot (Vasilescu et al, 2010). The basic layout incorporates four thrusters arranged in a symmetric cross in the stern pointing in forward direction – see Fig. 2. This allows direct control over the forward/backward movement along the robot's longitudinal axis, the pitch angle and the yaw angle. All four motors work in combination for acceleration/deceleration. Additionally two vertically mounted thrusters control depth and the roll angle.

A low-level control unit, based on an autopilot board by Ascending Technologies, is the central hub for the embedded systems and controls the 6-dimensional (6D) motion underwater. It consists of two 60 MHz ARM7 RISC processors; one of them is freely programmable. The other one combines three micro-electro-mechanical systems (MEMS) gyroscopes, a three-axis acceleration sensor, a three-axis magnetometer, and a pressure sensor to an inertia-force-measurement unit and pre-processes the data from these sensors.

The command unit of the high-level control can utilise this angular and translational data over a direct on-board link. The high-level control is done on a standard personal computer in a small form factor integrated in the robot. It provides the Robot Operating System (ROS) infrastructure to decide on the desired speed and direction, the processing of the sensor data, object avoidance and recognition, data logging and interfacing to command and control.

A land-based station can be used to monitor the status of the robot and to give new commands. Direct control of the movement of the robot is also possible via either a wiiMote, Joystick or keyboard. The robot can operate

tethered via a Cat5 Ethernet cable for a high bandwidth communication. Alternatively for untethered operation the link between command and control and the robot can be established via an acoustic modem by Tritech.

The ALL is described in detail in Sec. 4. The flow sensors are arranged in two equidistant array arranged to a cross on the frontal hemisphere with 17 sensors in total.

3.2 Model of the Dynamics of Snookie

As mentioned in the introduction to this section, for a proper design and control of the robot capable of manoeuvring on the basis of flow sensing, a careful description and analysis of the dynamics is crucial. Estimating the forces acting on a body in a fluid is a non-trivial problem. The traditional approach to describe the dynamics of bodies moving in fluids is an approximative analytic one. Such an approach delivers correct estimates of orders of magnitude and reasonable bounds of the relevant forces.

To avoid both, additional contributions due to the wave drag and complications in the calculation of the flow field due to a nonlinear boundary condition at the force-free surface, the robot is assumed to dive sufficiently deep. This condition is met in good approximation at a depth larger than five times the diameter of the moving object (Brennen, 1982, Sec. 3.8) below an undisturbed water surface. The forces acting on the body are empirically split up into contributions of viscous drag, pressure drag (also called form drag), lift, and increased inertia expressed by *added masses* as a consequence of the acceleration of displaced fluid. The viscous and pressure drag contributions may be considered as corrections due to viscosity of the stationary motion of a body in an ideal fluid, which otherwise would not experience any forces. The lift contribution stems from lifting surfaces with sharp trailing edges such as the fins. This decomposition is actually an attempt of a low order series approximation in velocity and acceleration of the forces acting on a body moving in an infinite viscous fluid initially at rest. In general, the drag as well as fluid inertia depend on the current and previous velocity and acceleration (Obasaju et al, 1988). Additional effects like Basset forces and drag and lift forces, arising from the shedding of vortices, which in principle can be accounted for by a semi-analytic model, are ignored throughout this work. The velocities and time constants of the motion of the robot, of course, guarantee incompressibility at any time. In the following subsections the force components are described and computed for *Snookie.*

All quantities measured and all action performed by the robot are with respect to the coordinate system of the robot, the *body-fixed system* (BFS). However, for self localisation, path planning and navigation, the robot also requires its own velocity and position, and the position and velocity of surrounding objects in a global frame, the *frame of reference* (FOR). It provides

an inertial system with the undisturbed fluid at rest. In the following section both frames, the relevant kinematic and dynamic quantities, and their transformations are briefly introduced.

3.2.1 Coordinate Frames of Reference

A suitable coordinate system for the description of the environment of *Snookie*, the FOR $\{e_X, e_Y, e_Z\}$, is fixed in space. It is an orthonormal inertial system. Stationary objects like the walls of a basin, which enter the fluid mechanics as boundary conditions, are fixed in space and therefore independent of time. The coordinate system is defined in a way, such that the directions e_X and e_Y are in the plane of the undisturbed water surface and e_Z is in positive direction pointing downwards into the fluid.
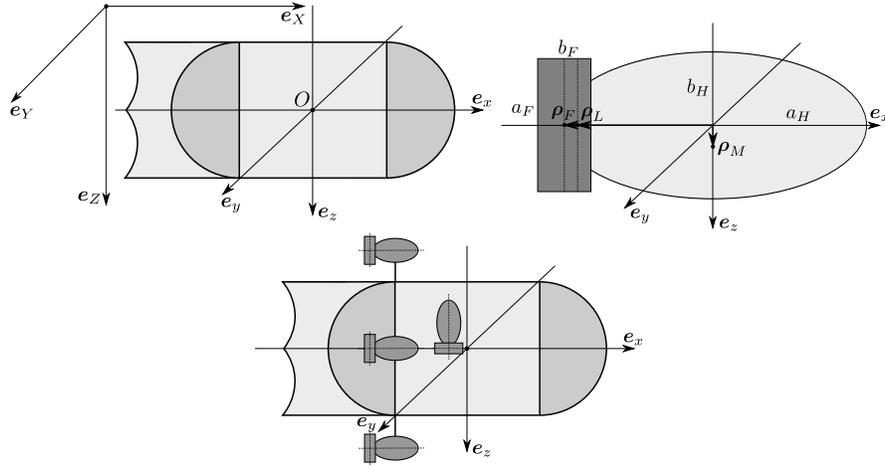
Fig. 2: *Left*: Frame of reference $\{e_X, e_Y, e_Z\}$ and body-fixed system $\{e_x, e_y, e_z\}$ with origin O at the geometric centre of the hull. *Right*: Geometry of the fluid-mechanically active parts of the robot with equivalent fin and equivalent hull without the thrusters. *Bottom*: Arrangement of the 6 thrusters in the body-fixed system of the robot.

The second coordinate system is the *BFS*, see Fig. 2. It is prescribed by the robot, a rigid body, carrying out arbitrary motion relative to the laboratory system. The system is orthonormal. It is defined by the basis vectors $\{e_x, e_y, e_z\}$. The orientation of the basis vector e_x of the BFS shall coincide with the longitudinal axis of *Snookie* pointing to the bow, the e_y direction points to the starboard side, and e_z is given by their cross product. The natural choice for the position of the origin O of the BFS, expressed in co-

ordinates of the FOR by the vector $\boldsymbol{O}$, is the *centre of mass* of a *rigid body*, since no coupling between rotational and translations degrees of freedom in the equations of motion (4) occurs in this system in the sense that resultant forces only affect the translational momentum and resultant torques only the angular momentum. For now, the real position of the centre of mass of the robot is unknown. A good choice for O is in the centre of volume of the hull of the robot. All quantities measured by devices on-board of *Snookie* are provided in the BFS. The state of a rigid body is fully described by the location and orientation of the BFS relative to the FOR. In order to clearly distinguish between a quantity expressed in the FOR and the same quantity in the BFS, capital symbols are used for coordinate vectors and matrices in the FOR $\{\boldsymbol{e}_X, \boldsymbol{e}_Y, \boldsymbol{e}_Z\}$ and lower symbols for the BFS $\{\boldsymbol{e}_x, \boldsymbol{e}_y, \boldsymbol{e}_z\}$.

The BFS may be rotated against the laboratory system, which is described by a modified set $\boldsymbol{\Phi} = (\Phi, \Theta, \Psi)$ of implicit Euler angles (Tait–Bryan angles). If the orientation of the body and the body-fixed basis vectors were initially parallel to the ones of the FOR, the following procedure describes the rotation of the body at a given instance of time. Rotate around $\boldsymbol{e}_Z$ about the yaw angle Ψ onto $\{\boldsymbol{e}'_X, \boldsymbol{e}'_Y, \boldsymbol{e}_Z\}$ with $-\pi < \Psi \leq \pi$. Next, perform a rotation around $\boldsymbol{e}'_Y$ about the pitch angle Θ onto $\{\boldsymbol{e}_x, \boldsymbol{e}'_Y, \boldsymbol{e}'_Z\}$ with $-\frac{\pi}{2} \leq \Theta \leq \frac{\pi}{2}$ and finally rotate around $\boldsymbol{e}_x$ about the roll angle Φ onto $\{\boldsymbol{e}_x, \boldsymbol{e}_y, \boldsymbol{e}_z\}$ with $-\pi < \Phi \leq \pi$. Then, the rotation $\boldsymbol{R}$ of a vector from the FOR to the BFS is given by

$$\boldsymbol{R} = \begin{pmatrix} 1 & 0 & 0 \\ 0 & \cos\Phi & \sin\Phi \\ 0 & -\sin\Phi & \cos\Phi \end{pmatrix} \begin{pmatrix} \cos\Theta & 0 & -\sin\Theta \\ 0 & 1 & 0 \\ \sin\Theta & 0 & \cos\Theta \end{pmatrix} \begin{pmatrix} \cos\Psi & \sin\Psi & 0 \\ -\sin\Psi & \cos\Psi & 0 \\ 0 & 0 & 1 \end{pmatrix} \tag{1}$$

and its inverse by $\boldsymbol{R}^{-1} = \boldsymbol{R}^T$. The definition of the Euler angles depends on the order in which the transformation is carried out and finite rotations are therefore not commutative. The angular velocities are computed from the Euler angles (Lewandowski, 2003) by

$$\boldsymbol{\Omega} = \begin{pmatrix} 1 & 0 & -\sin\Theta \\ 1 & \cos\Phi & \sin\Phi\cos\Theta \\ 0 & -\sin\Phi & \cos\Phi\cos\Theta \end{pmatrix} \begin{pmatrix} \dot{\Phi} \\ \dot{\Theta} \\ \dot{\Psi} \end{pmatrix} . \tag{2}$$

The total time derivative of a vector-valued quantity in an accelerated system expressed in BFS coordinates is given by

$$\frac{\mathfrak{D}}{\mathfrak{D}t} = \frac{\mathrm{d}}{\mathrm{d}t} + \boldsymbol{\omega} \times \tag{3}$$

with $\boldsymbol{\omega} = \boldsymbol{R}\boldsymbol{\Omega}\boldsymbol{R}^T$. The additional term $\boldsymbol{\omega}\times$ stems from the time derivative of the basis vectors of the accelerated BFS.

3.2.2 Rigid-Body Motion

As will be seen in Sec. 3.2.4, the fluid-mechanical forces on the body due to acceleration in an ideal fluid can be formulated in the framework of rigid body dynamics. Before the forces on the robot exerted by the fluid are treated in depth in the following sections, the inertial forces of the rigid body due to its body mass in the BFS shall be briefly introduced.

The velocity $\boldsymbol{V}$ of the origin O of the BFS expressed in coordinates of the BFS is denoted by $\boldsymbol{v}$, the angular velocity $\boldsymbol{\Omega}$ of the BFS about O by $\boldsymbol{\omega}$, the acceleration $\dot{\boldsymbol{V}}$ of O by $\boldsymbol{a}$, the angular acceleration by $\dot{\boldsymbol{\Omega}}$ and $\boldsymbol{\alpha}$, the moments of inertia $\boldsymbol{I}$ of the rigid body computed about its centre of mass by $\boldsymbol{\iota}$, and the position of the centre of body mass relative to O by $\boldsymbol{\rho}_M$. The mapping between the two systems is given by $\boldsymbol{O}$, $\boldsymbol{\Phi} = (\Phi, \Theta, \Psi)^T$, (1), and (2).

Instead of formulating the inertial force $\boldsymbol{f}^I$ and inertial torque $\boldsymbol{t}^I$ as a sum or integral over the inertial forces acting on each particle, especially in case of changing masses, it is easier to take the total time derivative of the momentum $\boldsymbol{m} = m(\boldsymbol{v} + \boldsymbol{\omega} \times \boldsymbol{\rho}_M)$ and the angular momentum $\boldsymbol{l} = \boldsymbol{\iota}\boldsymbol{\omega} + m\,\boldsymbol{s} \times (\boldsymbol{\omega} \times \boldsymbol{\rho}_M)$, where m is the body mass and $\boldsymbol{\iota}$ is the moment of inertia computed about the centre of mass $\boldsymbol{\rho}_M$ relative to O, which results in

$$\begin{pmatrix} \boldsymbol{f}^I \\ \boldsymbol{t}^I \end{pmatrix} = \begin{pmatrix} m\mathbb{1} & -m\boldsymbol{\rho}_M\times \\ m\boldsymbol{\rho}_M\times & \boldsymbol{\iota} - m\,\boldsymbol{\rho}_M\times \boldsymbol{\rho}_M\times \end{pmatrix} \begin{pmatrix} \boldsymbol{a} \\ \boldsymbol{\alpha} \end{pmatrix} + \begin{pmatrix} \boldsymbol{\omega} \times m\boldsymbol{v} \\ \boldsymbol{\omega} \times (\boldsymbol{\iota} - m\,\boldsymbol{\rho}_M\times \boldsymbol{\rho}_M\times)\,\boldsymbol{\omega} \end{pmatrix},$$
(4)

whereby the totally anti-symmetric matrix representation

$$\boldsymbol{c}\times = \begin{pmatrix} 0 & -c_3 & c_2 \\ c_3 & 0 & -c_1 \\ -c_2 & c_1 & 0 \end{pmatrix}$$
(5)

of a cross product $\boldsymbol{c}\times$ is used. Any other location of the origin of the BFS than the centre of mass couples linear and angular motion. Equation (4) incorporates Steiner's theorem (Meirovitch, 2004) – also called parallel axis theorem – through the transformation of the moments of inertia $\boldsymbol{\iota} - m\,\boldsymbol{\rho}_M\times \boldsymbol{\rho}_M\times$. With shifted centre of mass an external force resultant not only changes the velocity of the BFS but also induces a change in angular velocity. The same holds true for an external torque resultant.

The equations of motion (4) describing the change of momentum and angular momentum may be further unified to a single equation in a very compact notation, which will be extended in the following section to incorporate fluid-mechanical forces acting on the robot. By definition of the 6×6 mass matrix

$$\boldsymbol{\lambda} = \begin{pmatrix} m\mathbb{1} & -m\,\boldsymbol{\rho}_M\times \\ m\,\boldsymbol{\rho}_M\times & \boldsymbol{\iota} - m\,\boldsymbol{\rho}_M\times \boldsymbol{\rho}_M\times \end{pmatrix},$$
(6)

the anti-symmetric 6×6 matrix

$$\boldsymbol{\varpi}\times = \begin{pmatrix} \boldsymbol{\omega}\times & 0 \\ 0 & \boldsymbol{\omega}\times \end{pmatrix}, \tag{7}$$

where $\boldsymbol{\omega}\times$ denotes the anti-symmetric 3×3 matrix representation (5) of the cross product, the generalised 6D velocity vector $\mathbf{u} = (\boldsymbol{v}, \boldsymbol{\omega})$, and the generalised 6D force vector $\mathfrak{f} = \left(\boldsymbol{f}^I, \boldsymbol{t}^I\right)$, the equations of rigid body motion without external forces then yield

$$\mathfrak{f}^I = \frac{\mathfrak{D}\boldsymbol{\lambda}\mathbf{u}}{\mathfrak{D}t} = \frac{\mathrm{d}\boldsymbol{\lambda}\mathbf{u}}{\mathrm{d}t} + \boldsymbol{\varpi}\times\boldsymbol{\lambda}\mathbf{u} = 0\,. \tag{8}$$

3.2.3 Motion in an Ideal Fluid

Inertia forces cannot be neglected in comparison to drag forces. However, not only the robot itself but also the fluid displaced by the robot needs to be accelerated. The contribution of the displaced fluid to inertia in general depends on the flow field around the robot, which in turn depends on the initial state of the surrounding fluid, the shape of the moving body, the surrounding boundary conditions and in general on the Reynolds number. Some of the difficulties can be rendered inactive by a proper choice of the settings. *Snookie* is supposed to move through an unbounded fluid that is initially at rest. For the almost symmetric flow field around an ellipsoid without distortion by the thrusters, a good and straightforward mathematical description of the forces acting on the accelerated robot is available (Lewandowski, 2003).

For the case of a rigid body moving with translational velocity $\boldsymbol{V}$ and rotational velocity $\boldsymbol{\Omega}$ through an inviscid, incompressible, and unbounded fluid $\mathcal{D}$ initially at rest, the velocity $\boldsymbol{U} = \nabla\Phi$ of the fluid is fully described by the velocity potential Φ fulfilling (Lamb, 1945)

$$\Delta\Phi = 0 \tag{9}$$

on $\mathcal{D}$ and the no-penetration condition

$$\left.\frac{\mathrm{d}\Phi}{\mathrm{d}N}\right|_{\mathcal{S}} = (\boldsymbol{V} + \boldsymbol{\Omega}\times\boldsymbol{R})\cdot\boldsymbol{N} \tag{10}$$

at any point $\boldsymbol{R}$ on the surface $\mathcal{S}$ of the rigid body and the corresponding unit surface normal $\boldsymbol{N}$ inward $\mathcal{D}$. The velocity potential is supposed to vanish at infinity. Following the naming conventions from Sec. 3.2.1, capital symbols denote quantities with respect to the FOR. Therefore, $\boldsymbol{R}$ and $\boldsymbol{N}$ are functions of time. The time course of Φ is solely given by the right hand side of (10). The potential Φ is a linear function of the velocity of the surface of the moving body.

3.2.4 Added Masses

The linearity of (9) and the linearity of Φ in the translational and rotational velocities of the body (10) allows to separate the potential into

$$\Phi = V_X \varphi_1 + V_Y \varphi_2 + V_Z \varphi_3 + \Omega_X \varphi_4 + \Omega_Y \varphi_5 + \Omega_Z \varphi_6 \,. \tag{11}$$

After the separation, given the setting described in Sec. 3.2.3, the harmonic functions φ_i do not depend on the velocity of the moving body any more, just on its shape, since

$$\left. \frac{\mathrm{d}\varphi_i}{\mathrm{d}N} \right|_{\mathcal{S}} = N_i \;\; \text{for} \;\; i = 1, 2, 3 \;\; \text{and} \;\; \left. \frac{\mathrm{d}\varphi_i}{\mathrm{d}N} \right|_{\mathcal{S}} = (\boldsymbol{R} \times \boldsymbol{N})_{i-3} \;\; \text{for} \;\; i = 4, 5, 6 \,, \tag{12}$$

and the choice of the coordinate system they are computed in. For the a simpler notation the translational and rotational velocities are gathered in the 6D velocity vector $\boldsymbol{\mathcal{U}} = (\boldsymbol{V}, \boldsymbol{\Omega})$ as in Sec. 3.2.2, and the potential is given by

$$\Phi = \sum_{i=1}^{6} \mathcal{U}_i \varphi_i \,. \tag{13}$$

The kinetic energy stored in the flow field $\nabla \Phi$ around the moving body

$$T = \frac{1}{2} \varrho \int_{\mathcal{D}} |\nabla \Phi|^2 \, \mathrm{d}V$$

can be rewritten using Green's second identity as $T = \frac{1}{2} \lambda_{ij} \mathcal{U}_i \mathcal{U}_j$ with the coefficients

$$\lambda_{ij} = -\varrho \oint_{\mathcal{S}} \frac{\partial \varphi_i}{\partial N} \varphi_j \mathrm{d}S \,. \tag{14}$$

The effects of the ideal incompressible irrotational fluid on the motion of the body are fully accounted for by additional inertia λ_{ij} (Kirchhoff, 1870; Korotkin, 2010), the so called *added-masses.*

3.2.5 Added Mass Matrix under Coordinate Transformations

For the sake of simplicity, the added mass matrix $\boldsymbol{\lambda}$ is computed with respect to the point of maximum symmetry. It is usually necessary to adapt $\boldsymbol{\lambda}$ to a given geometry, e.g., shift the axis of rotation, since other constraints such as the choice of the origin of the BFS force the body to rotate around a different point than the one assumed for the computation of the added masses.

   The kinetic energy of the flow field around the body must be invariant under a change of the coordinate system the added masses are computed in. All the summands are quadratic forms of the velocities. The idea of the derivation of the transformation formulas for the added masses is to express

the kinetic energy of the flow field in a new coordinate system and collect all term of a certain product $\mathcal{U}_i\mathcal{U}_j$. The coefficients are the added masses in the new system.

In the most general case the new system $\{\boldsymbol{e}_x, \boldsymbol{e}_y, \boldsymbol{e}_y\}$ is shifted by the vector $\boldsymbol{\xi}$, moves with velocity $\boldsymbol{V}$, and rotates about its origin with angular velocity $\boldsymbol{\Omega}$ relative to the old system $\{\boldsymbol{e}_X, \boldsymbol{e}_Y, \boldsymbol{e}_Z\}$. Due to the analogy to the transformation between a FOR and a BFS, the same notation as in Sec. 3.2.2 is used. The added masses shall be known in the system $\{\boldsymbol{e}_X, \boldsymbol{e}_Y, \boldsymbol{e}_Z\}$, and are supposed to be determined in $\{\boldsymbol{e}_x, \boldsymbol{e}_y, \boldsymbol{e}_y\}$. The velocity expressed in coordinates of the new system is given by $\boldsymbol{u} = \boldsymbol{R}(\boldsymbol{V} + \boldsymbol{\Omega} \times \boldsymbol{\xi})$ with rotation matrix $\boldsymbol{R}$ as defined by (1). Again, 6D vectors are used to express the velocity of the new system in coordinates of the old $\mathcal{U} = (\boldsymbol{V}, \boldsymbol{\Omega})$ and new $\mathfrak{u} = (\boldsymbol{v}, \boldsymbol{\omega})$ system. Written component-wise the transformation of the velocity and angular velocity is given by

$$\mathcal{U}_{i=1..3} = \sum_{m=1}^{3} \mathfrak{u}_m R_{mi} - \varepsilon_{ijk}\Omega_j\xi_k \quad \text{and} \quad \mathcal{U}_{3+i} = \sum_{m=1}^{3} \mathfrak{u}_m R_{mi} \text{ for } i = 1, 2, 3$$

with the Levi-Civita symbol ε_{ijk}, and the transformation matrix $R_{mn} = \boldsymbol{e}'_m \cdot \boldsymbol{e}_n$, where $m \in \{x, y, z\}$ and $n \in \{X, Y, Z\}$.

The transformation of the added masses turns out to be quite simple, if the coordinate transformation consists of just a shift about $\boldsymbol{\xi}$, i.e. a shift of the axis of rotation by $-\boldsymbol{\xi}$, and if the added mass matrix to be transformed has diagonal shape. This means that the original mass matrix was computed about the centre of the fluid-mechanical forces acting on the body and the axes of the BFS coincide with the principal axes of the moment of inertia submatrix of the added mass tensor. The transformation directive becomes $\lambda'_{mn} = \lambda_{mn}$ for $m = n = 1, 2, 3$; $\lambda'_{15} = -\lambda_{11}\xi_3$, $\lambda'_{24} = \lambda_{22}\xi_3$, $\lambda'_{34} = -\lambda_{33}\xi_2$, $\lambda'_{35} = \lambda_{33}\xi_1$, $\lambda'_{16} = \lambda_{11}\xi_2$, and $\lambda'_{26} = \lambda_{22}\xi_1$ for $m = 1, 2, 3$ and $n = 4, 5, 6$ or $m = 4, 5, 6$ and $n = 1, 2, 3$; $\lambda'_{44} = \lambda_{44} + \lambda_{22}\xi_3^2 + \lambda_{33}\xi_2^2$, $\lambda'_{45} = -\lambda_{33}\xi_1\xi_2$, $\lambda'_{46} = -\lambda_{22}\xi_1\xi_3$, $\lambda'_{55} = \lambda_{55} + \lambda_{33}\xi_1^2 + \lambda_{11}\xi_3^2$, $\lambda'_{56} = -\lambda_{11}\xi_2\xi_3$, and $\lambda'_{66} = \lambda_{66} + \lambda_{11}\xi_2^2 + \lambda_{22}\xi_1^2$ for $m = 4, 5, 6$ and $n = 4, 5, 6$. Any entry not covered by the symmetry of $\boldsymbol{\lambda}$ and not listed vanishes. A careful comparison of the transformed added masses with the inertia of a rigid body (4) shows, that the added masses behave like body masses in every way. These properties of the added masses are a consequence of the fact, that the potential of the flow field around the moving rigid body is a linear function of the translational and rotational velocity of the moving body.

In Sec. 3.2.9 the *total inertia* of *Snookie* will be composed from the body mass and inertia and the added masses of independent geometrical primitives, resembling the fluid-mechanically active parts of the robot – see Fig. 2, using these transformation directives for added masses.

3.2.6 Forces on the Hull

As discussed in section Sec. 3.2.4, the favourable system to compute the added masses is a body-fixed frame of reference using all available symmetries. For the purpose of computational simplicity we shall approximate the trunk of *Snookie* by a prolate spheroid with long axis $2a_H$ and short axis $2b_H$, whose axis of revolution lies along the x-axis, with a being the semi-length of the axis and b the radius in the equatorial plane at $x = 0$. Then, the added masses with respect to the geometric centre of the ellipsoid are given by (Newman, 1977, pp 144)

$$m_{H1} := \lambda_{11} = \frac{4}{3}\pi\varrho a_H b_H^2 \frac{\alpha_H}{2 - \alpha_H}\,, \qquad m_{H2} := \lambda_{22} = \lambda_{33} = \frac{4}{3}\pi\varrho a_H b_H^2 \frac{\beta_H}{2 - \beta_H}\,,$$

$$\iota_H := \lambda_{55} = \frac{4}{3}\pi\varrho a_H b_H^2 \left(a_H^2 + b_H^2\right) \frac{e^4 \left(\beta_H - \alpha_H\right)}{(2 - e^2)\left[2e^2 - (2 - e^2)\left(\beta_H - \alpha_H\right)\right]}\,,$$

$$\lambda_{66} = \lambda_{55}\,, \qquad \lambda_{44} = 0\,, \qquad \text{and} \qquad \lambda_{ij} = 0 \quad \text{for} \quad i \neq j\,, \tag{15a}$$

where

$$\alpha_H = \frac{2(1 - e^2)}{e^3}\left[\frac{1}{2}\ln\left(\frac{1 + e}{1 - e}\right) - e\right]\,, \qquad \beta_H = \frac{1}{e^2} - \left(\frac{1 - e^2}{2e^3}\right)\ln\left(\frac{1 + e}{1 - e}\right)\,,$$

$$e^2 = 1 - \left(\frac{b_H}{a_H}\right)^2\,. \tag{15b}$$

The parameters a_H and b_H are chosen so that, first, the volume $V_E = 4/3 a_H b_H^2$ of the prolate spheroid is equal to the volume of the trunk of *Snookie* consisting of the water tight cylinder and the two semi-spheres at the bow and the stern. And second, the surface of the ellipsoid

$$S_E = 2\pi b_H^2 + \frac{2\pi a_H b_H}{\sqrt{1 - \frac{b_H^2}{a_H^2}}} \sin^{-1}\left(\sqrt{1 - \frac{b_H^2}{a_H^2}}\right)$$

has to be equal to the surface of *Snookie* $S_H = 4\pi R^2 + 2\pi R(L - 2R)$. Numerical solution of these two conditions yields $a_H = 41.484\,\mathrm{cm}$ and $b_H = 13.620\,\mathrm{cm}$. The added masses are $m_{H1} = 5.922\,\mathrm{kg}$ and $m_{H2} = 23.573\,\mathrm{kg}$, the added moment of inertia $\iota_H = 1.822\,\mathrm{kg\,m}^2$.

The viscosity induced drag on the surface of the moving body is hard to determine analytically and usually described by empirical drag coefficients (Panton, 2005). The main drag on *Snookie* stems from the separation of the boundary layer around the hull and the breaking of the symmetry of the flow field, which finally leads to a wake with reduced pressure at the stern. For *Snookie* different drag force is expected for forward and sideward motion

$$F_{fd} = -\frac{1}{2}\varrho\, C_{fd} A_H \left| u_x \right| u_x\,, \quad \boldsymbol{F}_{sd} = -\frac{1}{2}\varrho\, C_{sd} B_H \begin{pmatrix} u_y \\ u_z \end{pmatrix} \sqrt{u_y^2 + u_z^2}\,, \quad (16)$$

where C_{fd} and C_{sd} are the forward and sideward drag coefficients and $A_H = \pi R^2$ and $A_B = \pi R^2 + 2R\,(L - 2R)$ the respective cross-sections with $L = 74\,\mathrm{cm}$ being the overall length and $R = 12.5\,\mathrm{cm}$ the radius of the robot. The total pressure drag is approximated by a linear composition (Newman, 1977, pp. 13) of forward and sideward drag. It acts on the geometric centre of the hull, the origin O of the BFS. The drag coefficient is a non-trivial function of the Reynolds number. It varies e.g. for a circular cylinder between $C \approx 20$ at Re $= 1$ and $C \approx 1.1\ldots 1.3$ at Re $= 1000$. In absence of measured data and better assumptions, forward and sideward drag coefficients are set to $C_{fd} = C_{sd} = 0.3$. For the Reynolds numbers considered here, this value is a safe estimate of the lower bound of the pressure drag coefficient of a sphere (Oertel and Mayes, 2004, pp. 161). Overestimation of the pressure drag would lead to underestimated thruster forces required to stop the robot when an obstacle appears. The drag on the robot due to rotation is neglected, since in general high angular velocities are not intended to occur. The drag force on the hull $\boldsymbol{d}_H = (F_{fd}, \boldsymbol{F}_{sd})$ acts opposite to the direction of motion with force resultant attacking at the geometric centre of the hull and does not produce any torque. Thus, the resultant drag force vector of the hull is given by $\mathfrak{f}_H = (\boldsymbol{d}_H, \boldsymbol{0})^T$.

3.2.7 Forces on the Fins

The motion of an elongated blunt body like *Snookie* in the direction of its main axes, even if it were perfectly symmetric with respect to the main axis and the fluid were perfectly at rest, is unstable. Any small disturbance in pitch or yaw causes torque about the centre of mass, called Munk's moment (Lewandowski, 2003, pp 39), throwing the body out of the desired trajectory. The yaw and pitch instability of forward motion is balanced by a vertical and a horizontal fin at the stern of *Snookie*. The fins consist of thin plates of length $20.2\,\mathrm{cm}$ and height $b_F = 2R = 25\,\mathrm{cm}$ equal to the diameter of the robot, with a cut-out for the spherical stern. This results in an effective surface of $260\,\mathrm{cm}^2$ per fin with a mean effective length of each fin $a_F = 10.4\,\mathrm{cm}$. The geometric centre of the rectangular equivalent fin is located $l_h = 39.3\,\mathrm{cm}$ behind the geometric centre of the hull. The vertical and horizontal fin are arranged to form a symmetric cross like shape.

The incident flow to the fins is taken to be homogeneous at large distance, and it is assumed that it is not affected by the presence of the hull or the thrusters. The relative velocity between fin and undisturbed fluid is approximated by the velocity $\boldsymbol{u}_F = -\boldsymbol{v} - \boldsymbol{\omega} \times \boldsymbol{\rho}_F$ of the geometric centre of the fin. Analytic expressions are available for the lift on a 2D cross section of a plate of zero thickness and cord length l in in an homogeneous free

stream and angle of attack α (Breslin and Andersen, 2008, pp 66). The circulation around a cross section of the fin according to the 2D theory is given by $\Gamma_F = \pi a_F u_F \sin \alpha$, which results in the total lift $F_F = \pi \varrho A_F u^2 \sin \alpha$ on the fin with fin area $A_F = a_F b_F$. In 3D the lift on a plate of finite length h is overestimated depending on the ratio h/l. Due to the absence of analytic expressions for the full 3D case, the 2D expression is widely used for hydrofoils. The section of the plate also experiences a torque $T_L = 1/4 \pi \varrho A_F^2 \sin \alpha$ per unit length about the centre of pressure forces at the so called quarter-cord point, located halfway between the leading edge and the centre line of the fin. The quarter-cord point of the fins is located at $\boldsymbol{\rho}_Q = (-36.7, 0, 0)^T$ cm behind the geometrical centre O of the hull on the long axis of the robot. The occurring torques on the fin are balanced by the mounting and do not affect the dynamics.

The z (y) component of the incident flow due to the presence of the horizontal (vertical) fin does not significantly contribute to the lift produced by the vertical (horizontal) fin. The incident flow $\boldsymbol{u}_F$ is therefore decomposed into the lift producing components $\boldsymbol{u}_V = \boldsymbol{u}_F - (\boldsymbol{u}_F \cdot \boldsymbol{e}_z)$ for the vertical and the horizontal fin $\boldsymbol{u}_H = \boldsymbol{u}_F - (\boldsymbol{u}_F \cdot \boldsymbol{e}_y)$. With the angles $\sin \alpha_V = (\boldsymbol{u}_V \cdot \boldsymbol{e}_y) / \|\boldsymbol{u}_V\|$ and $\sin \alpha_H = (\boldsymbol{u}_H \cdot \boldsymbol{e}_z) / \|\boldsymbol{u}_H\|$ between the fin and the lift producing components of the incident flow an estimate of the lift on the vertical and horizontal fin, acting on the quarter-cord point $\boldsymbol{\rho}_Q$ is given by

$$\boldsymbol{l}_V = \tilde{A}_F \sin \alpha_V \|\boldsymbol{u}_V\| \begin{pmatrix} -u_{Vy} \\ u_{Vx} \\ 0 \end{pmatrix} \text{ and } \boldsymbol{l}_H = \tilde{A}_F \sin \alpha_H \|\boldsymbol{u}_H\| \begin{pmatrix} -u_{Hz} \\ 0 \\ u_{Hx} \end{pmatrix} \quad (17)$$

with $\tilde{A}_F = -\pi \varrho a_F b_F$. These results are applicable within an range of $\alpha = -10° \ldots 10°$ (Newman, 1977, pp 20), provided the plate has a smooth surface. The breakdown of the lift at higher angles of attack due to stall is accounted for by an additional factor of $\Theta(\alpha_0 - \alpha) \Theta(\alpha_0 + \alpha)$ for the respective force components with Θ being the Heaviside step function and α_0 the critical angle. The lift forces on the quarter cord-point have the force and torque resultants

$$\boldsymbol{f}_L = \boldsymbol{l}_V + \boldsymbol{l}_H \qquad \text{and} \qquad \boldsymbol{m}_L = (\boldsymbol{l}_V + \boldsymbol{l}_H) \times \boldsymbol{\rho}_Q \qquad (18)$$

about O, which may be combined for a compact notation to the 6D force vector $\mathfrak{f}_L = (\boldsymbol{f}_L, \boldsymbol{m}_L)^T$. As mentioned previously, the effective lift of hydrofoils or wings of finite length is reduced in 3D contrary to the 2D results due to the flow over the tip of the wing. The lift therefore enters the equations of motion in the dynamical model with an additional safety margin of $1/2$ to ensure that the stabilising effects of the fins are not overestimated.

Viscosity induced pressure drag on the fins in x direction is modelled due to the absence of better alternatives by the drag coefficient $C_P = 1.28$ on a flat plate perpendicular to the incident flow $F_P = \frac{1}{2} C_P \varrho \hat{A}_F u^2$, corrected by

the net frontal area $\hat{A}_F = a_F b_F \sin(\alpha)$ exposed to the incident flow, which is also taken as as a rough estimate for the lift induced drag for $|\alpha| < 10°$.

Correct estimates of the drag on the fins due to sideward motion or rotations are challenging. Since lift and drag scale with u_F^2, an error in the estimates of these forces does not cause large effects on the dynamics, since in general the rotational velocity of the robot is small. Drag coefficients of similar shapes, e.g. a cube, a cube at an angle of 45°, and a circular cylinder, are in the range of $0.8 \ldots 1.3$ for Reynolds numbers Re ≈ 1000. A safe estimate of the lower bound of the drag forces of the fins at sideward or vertical motion is therefore given by the drag coefficient $C_F \approx 1$ of a cylinder with the net frontal area of the fin A_F with mathematically convenient independence of the roll angle. The drag of the fin acts upon the geometric centre of the fin located at $\boldsymbol{\rho}_F$. The incident flow $\boldsymbol{u}_F$ is decomposed in the x component and the components perpendicular to the fins $u_{Fy} = \boldsymbol{e}_y \cdot \boldsymbol{u}_F$ and $u_{Fz} = \boldsymbol{e}_z \cdot \boldsymbol{u}_F$, and the drag on the fins is given by

$$
\boldsymbol{d}_F = -\frac{1}{2}\varrho C_F A_F \sqrt{u_{Fy}^2 + u_{Fz}^2}
\begin{pmatrix} 0 \\ u_{Fy} \\ u_{Fz} \end{pmatrix} .
\tag{19}
$$

The resulting force and torque $\mathfrak{f}_F = (\boldsymbol{f}_F, \boldsymbol{m}_F)^T$ on the origin O of the BFS are

$$
\boldsymbol{f}_F = F_P \boldsymbol{e}_x + \boldsymbol{d}_F \qquad \text{and} \qquad \boldsymbol{m}_F = \boldsymbol{f}_F \times \boldsymbol{\rho}_F . \tag{20}
$$

The fins stabilise the forward motion. Their disadvantage are increased added masses constraining the manoeuvrability. The added masses of the perpendicular arrangement of the vertical and horizontal fin is approximated by the 2D result of a cross-shaped section composed of plates of zero thickness. Both the plates have a length of $a_F = 10.4\,\text{cm}$ and a width of $b_F = 25\,\text{cm}$. The added masses per unit length cross section (Newman, 1977, pp 144) are given by $\lambda_{11} = 0$, $\lambda_{22} = \lambda_{33} = \pi\varrho(l/2)^2$, $\lambda_{44} = 2/\pi\varrho(h/2)^4$, and $\lambda_{55} = \lambda_{66} = 1/8\pi\varrho(l/2)^4$, which results in the added masses

$$
m_F = \lambda_{22} = \lambda_{33} = \pi\varrho\frac{a_F b_F^2}{4} , \quad \iota_{F1} = \lambda_{44} = \varrho\frac{b_F^4 a_F}{8\pi} ,
$$
$$
\iota_{F2} = \lambda_{55} = \lambda_{66} = \varrho\frac{\pi a_F^4 b_F}{128}
\tag{21}
$$

of the cross shaped fins computed about their common geometric centre. Their numerical values are $m_F = 5.105\,\text{kg}$, $\iota_{F1} = 16.16 \cdot 10^{-3}\,\text{kg m}^2$, and $\iota_{F2} = 0.718 \cdot 10^{-3}\,\text{kg m}^2$.

Vertical motion remains unstable since the motion in $\boldsymbol{e}_z$-direction cannot be stabilised by fixed fins without affecting motions in $\boldsymbol{e}_x$-direction. During submerging and descending Munk's moment appears due to both, the round

shape of the bow and the large angle of a attack at the tip of the fin. Since the vertical speed is usually small, the thrust needed for balancing is also small.

3.2.8 Thrusters

The thrusters are neglected in the computation of the added masses, the drag, and the lift. They provide the robot with acceleration in forward / backward and vertical direction, and also angular momentum about pitch, roll, and yaw. The thrusters enter the equations of motions via the force generated by the propellers.

The four horizontal thrusters are placed at $\boldsymbol{\rho}_{Ti} = (l_H, \pm r_H/\sqrt{2}, \pm r_H/\sqrt{2})$ with $i \in \{1, 2, 5, 6\}$ symmetrically in a plane $l_H = 22.0\,\mathrm{cm}$ behind the geometric centre of the hull parallel to the $\boldsymbol{e}_y$-$\boldsymbol{e}_z$ plane in $\boldsymbol{e}_x$ direction at a distance of $r_H = 18.5\,\mathrm{cm}$ to the longitudinal axis of the hull – see Fig. 2. The two vertical thruster are located at $\boldsymbol{\rho}_{T3} = (s_{Vx}, r_V, 0)$ and $\boldsymbol{\rho}_{T4} = (s_{Vx}, -r_V, 0)$ symmetrically in a plane parallel to the $\boldsymbol{e}_y - \boldsymbol{e}_z$ plane at $\boldsymbol{\rho}_V = (s_{Vx} = -6.2, \pm r_V = \pm 19.0, 0)$ cm in $\boldsymbol{e}_z$ direction. The added masses of the hull and the fins depend of the direction of motion, therefore the total centre of mass also depends on the direction on motion – see Sec. 3.2.9. Any other arrangement of the vertical thrusters would effectively cause angular momentum about the y axis at pure vertical motion.

So far, a fairly simple thruster model is used. Thrust, torque, and efficiency not only depend on the geometry of the propeller, but also on the relative speed u_T of the incident flow and the rotation number ν of the axle, usually expressed in terms of the advance ratio $J = u_T/\nu d$ with diameter d of the propeller. The thrust $T = K_T(J)\,\varrho\nu^2 d^4$ and the torque $Q = K_Q(J)\,\varrho\nu^2 d^5$ of the propeller are determined by non-dimensional parameters, the thrust coefficient K_T and the torque coefficient K_Q, both functions of J (Newman, 1977; Breslin and Andersen, 2008), representing the specific properties of the propeller. The thrust and torque coefficient have their maximum and the smallest slope at zero advance ratio. The focus of the robot is put on slow motion and high acceleration. Accordingly, the coefficients were taken to be constant. It was further assumed, that a unique relations between pulse width and thrust force in the regime of $0 \ldots 2\,\mathrm{m/s}$ incident flow velocity exists. This is acceptable for small advance ratios.

Figure 3 shows the measured non-linear characteristic line of thrust force in both directions for a thruster with a three-blade 50 mm diameter propeller. Measurements were carried out with a thruster mounted on a JR3 six axis force-torque sensor. It automatically sweeps through the PWM of the motor driver, which results approximately in a current control of the motor for low advance ratios. Since the motor control is open-loop and friction of the seals, inertia, and viscosity keep the motor on hold for small PWM signals, a dead zone with no thrust exists, which can be clipped. The resulting characteristic

line for forward and backward thrust is fitted with a 2nd-order polynomial function. The forward T_f and backward T_b thrust are given by

$$T_f = 2 \cdot 10^{-4}x^2 + 1.11 \cdot 10^{-2}x - 1.186 \cdot 10^{-1} \quad \text{and} \tag{22}$$

$$T_b = 10^{-4}x^2 + 3.4 \cdot 10^{-3}x - 3.5 \cdot 10^{-2} \tag{23}$$

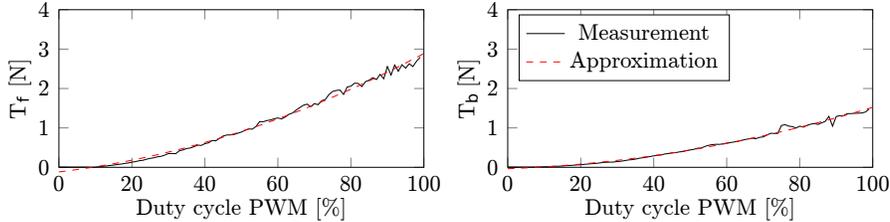with $x \in [0, 100]$ for the PWM duty cycle. Since the prediction made by

Fig. 3: *Solid line*: measured forward (*left*) and reverse (*right*)) thrust. *Dashed line*: 2nd order polynomial approximation.

the simple motion controller on how the pulse width will affect the state of motion of the robot is approximated to lowest order, this approach comes with sustaining demands for control activity and therefore increased power supply.

The external forces and torques acting on the total centre of mass given the current thrust T_i of the thrusters $i = 1 \ldots 6$ are given by

$$\boldsymbol{f}_T = \sum_{i \in \{1,2,5,6\}} T_i \, \boldsymbol{e}_x - \sum_{i \in \{3,4\}} T_i \, \boldsymbol{e}_z \qquad \text{and}$$

$$\boldsymbol{m}_T = \sum_{i \in \{1,2,5,6\}} T_i \boldsymbol{e}_x \times \boldsymbol{\rho}_{Ti} - \sum_{i \in \{3,4\}} T_i \, \boldsymbol{e}_z \times \boldsymbol{\rho}_{Ti} \,. \tag{24}$$

The respective 6D force vector is denoted by $\mathfrak{f}_T = (\boldsymbol{f}_T, \boldsymbol{m}_T)$.

3.2.9 Combination of Mass, Moment of Inertia and Added Masses

Snookie is buoyancy neutral, meaning that its mass is equal to the equivalent volume of water. But the mass is not distributed homogeneously. Counterweights are mounted below the longitudinal axis so that the robot is balanced about the pitch axis including fins and thrusters, and stable about the roll axis. The symmetry with respect to the vertical plane is preserved. The mass of *Snookie* including balancing weights and the flooded bow and stern is equal to its water displacement, $m = 32.324 \, \text{kg}$. The actual centre of mass is shifted below the origin O of the BFS by the vector $\boldsymbol{\rho}_M = (0, 0, \rho_M)$. Integration

over the mass distribution carried out by the computer aided design (CAD) program SolidWorks leads to a centre of mass $\boldsymbol{\rho}_M = (0, 0, 1.5)^T$ cm and moments of inertia $\iota_{11} = 0.23$, $\iota_{22} = 1.68$, $\iota_{33} = 1.70$, and $\iota_{ij} = 0$ for $i \neq j$ in units of kg m² computed in body-fixed coordinates about the centre of mass. Accordingly, the axis of rotation must be shifted by $-\boldsymbol{\rho}_M$,

$$\boldsymbol{\lambda}'_M = \begin{pmatrix} m \, \mathbb{1} & -m \, \boldsymbol{\rho}_M \times \\ m \, \boldsymbol{\rho}_M \times & \boldsymbol{\iota} - m \, \boldsymbol{\rho}_M \times \boldsymbol{\rho}_M \times \end{pmatrix} , \tag{25}$$

which was already incorporated in the inertia of the rigid body in Sec. 3.2.2.

The added mass matrices have been determined with respect to the geometric centre of each shape independently and now have to be transformed and combined according to their location in the BFS relative to O – see Sec. 3.2.5. The added mass matrix of the hull (15a) is already computed about the origin of the BFS and does not need any further treatment. The coordinate systems of the added mass matrix of the fin (21) has to be shifted by $-\boldsymbol{\rho}_F$. The resulting total mass matrix is given by

$$\boldsymbol{\lambda} = \boldsymbol{\lambda}'_M + \boldsymbol{\lambda}'_H + \boldsymbol{\lambda}'_F \tag{26}$$

with the entries $\lambda_{11} = m + m_{H1}$, $\lambda_{22} = m + m_{H2} + m_F$, $\lambda_{33} = \lambda_{22}$, $\lambda_{15} = \lambda_{51} = -\lambda_{24} = -\lambda_{42} = -m\rho_M$, $\lambda_{26} = \lambda_{62} = -\lambda_{35} = -\lambda_{53} = -m_F\rho_F$, $\lambda_{44} = \iota_{11} + m\rho_M^2 + \iota_{F1}$, $\lambda_{66} = \iota_{22} + m\rho_M^2 + m_F\rho_F^2 + \iota_H + \iota_{F2}$, $\lambda_{55} = \iota_{33} + m_F\rho_F^2 + \iota_H + \iota_{F2}$. The remaining entries of $\boldsymbol{\lambda}$ vanish.

A closer look at the combined added masses reveals, that for example the volume displaced by the hull, and therefore also the added mass (15a), depends on the direction of motion. The net frontal area for forward motion is much smaller than the net frontal area for sideward motion, and accordingly the displaced fluid. The centre of total mass for pure forward motion for example is given by

$$\boldsymbol{s}_F = \left(0, 0, \frac{m\rho_M}{m + m_{H1}} \right)^T , \tag{27}$$

the centre of total mass for pure sideward or vertical motion by

$$\boldsymbol{s}_V = (s_{Vx}, 0, s_{Vz})^T = \left(\frac{m_F\rho_F}{m + m_{H2} + m_F}, 0, \frac{m\rho_M}{m + m_{H2} + m_F} \right)^T . \tag{28}$$

Obviously, the centre of total mass has its own dynamics coupled to the motion of the robot. Strictly speaking, in the presence of added masses *Snookie* is not a rigid body any more. Although the position of each mass contribution, i.e. the added masses of the hull, the added mass of the fin, and body mass is fixed in the BFS, the centre of total mass moves since the quantity of the added masses – their relative weights in the barycentre – change with the direction of motion. With the origin of the BFS fixed in an arbitrary point on the rigid body, e.g. O, the location of the masses is fixed, and the equations

of motion of the rigid body can be used, keeping in mind that the total mass depends on the direction of motion.

3.2.10 Rigid-Body Motion with Drag, Lift and Thrust

The only thing left to do now is to balance the inertial forces of the rigid body (8) complemented by the added masses (26) with the origin of the BFS at the geometric centre of hull

$$\frac{\mathfrak{D}\boldsymbol{\lambda}\mathbf{u}}{\mathfrak{D}t} = \boldsymbol{Q} \tag{29}$$

with the external forces

$$\boldsymbol{Q} = (\mathfrak{f}_L + \mathfrak{f}_F + \mathfrak{f}_H + \mathfrak{f}_T)^T \ , \tag{30}$$

consisting of lift, drag, and thrust, which results in the standard equations of submarine motion (Newman, 1977; Feldman, 1979; Fossen, 1994). These equations can be solved easily by numerical integration in real-time on recent hardware (Sosnowski et al, 2010). The transformation of all dynamical quantities to the FOR is given in Sec. 3.2.1.

3.2.11 Validity and Benefit of the Model of the Dynamics

Numerous assumptions and simplifications have been made to arrive at equation (29). The most important ones shall be briefly reviewed and discussed. The assumptions and approximation were necessary to obtain a treatable model of the dynamics of the robot. The model is far from being perfect since there is no easy solution for the forces exerted on the robot by the surrounding fluid. However, it provides reasonable estimates of the dynamics at low computational efforts.

As briefly discussed in the introduction to Sec. 3.2, the model is restricted to the motion of the robot in an unbounded inviscid irrotational fluid at rest. No location dependent fluid-mechanical forces like additional pressure forces due to the presence of a wall (Korotkin, 2010; Nie et al, 2013) on the robot exist. The state of motion is fully determined by the translational and rotational velocity. In case additional boundaries were present, the added masses of *Snookie*, if computable at all, had to be adapted by an expression dependent on the current position of the robot relative to all surrounding boundaries (Korotkin, 2010, ch. 4 and 5). The effects of stationary walls and a free surface are negligible at sufficiently large distances, typically larger than 5 or 10 times the size of the robot.

While the inertia due to the physical mass of the robot are obtained directly from CAD, the estimates of the added masses are composed from the

fluid-mechanical inertia of simple shapes resembling the shape of the robot. Each element is treated independently of the others including the thrusters, which means that in the model disturbances of the fluid caused by each element do not interfere. In future experiments, it is planned to determine the coefficients of the equations of motion experimentally. The conditions for the non-viscous estimates of the inertial forces are strictly only met e.g. at Reynolds numbers up to 10 or 15 or during the early stages of rapid acceleration from rest (Newman, 1977, pp. 34).

Especially, it is assumed that the disturbance of the flow field of the robot due to the action of the thrusters is negligible. This assumption is justified for small thrust values and large distances between the thruster and the hull, which is not fulfilled very well for *Snookie*. If one wanted to take the interactions of the thrusters with the hull and the fin into account, one had to deal with added masses depending on the state of all six thrusters in the equations of motions. The added masses could be estimated by 3D boundary-element method (BEM) simulations or tow car experiments, with the robot attached to a force meter as a function of the six current thrust values.

Nevertheless, as soon as additional boundaries like a free surface or a solid wall are present, possibly significant errors are made in the estimation of the added masses as well as in the estimates of forces generated by the thrusters and forces that result from changing added masses. The estimates of the order of magnitude of the thrust forces required to stop the robot due to the appearance of an obstacle in the range of the ALL, however, remains the same. The added masses are indeed increased in the vicinity of a stationary obstacle. But, without further external forces, the total kinetic energy of the robot remains constant, since the added masses are an effect of the motion in an inviscid irrotational and inviscid fluid. The robot and the fluid moving with the robot are decelerated to the same extent to which the add mass is increased while approaching the stationary object. The power necessary to reduce the kinetic energy within a certain distance remains unchanged, no matter if the robot moves close to a wall or in open water. Due to the presence of a wall not only decelerating forces, but also torque might be exerted onto the robot. Therefore, it should be taken care of sufficient thrust reserve.

Viscosity is accounted for by quasi-stationary semi-empirical drag coefficients. This approximation breaks down at high accelerations. Furthermore, the assumption that viscous drag forces just add linearly to inertial forces and that viscous forces can be decomposed into forward and sideward forces is only an approximation. The decomposition is correct in the special cases that the vehicle moves forward, sideward, upward, or downward.

Even if the model of the dynamics of the robot would be perfect, due to the a priori unknown environment of the robot, the motion controller must be flexible enough, react fast enough, and have enough power available to compensate for external effects such as changing boundary conditions like the presence of a wall.

3.3 Motor Control

The equations of motion (29) are the basis to set up a control strategy for the robot. The equations are independent of the position and the orientation of the robot, but nonlinearly couple the velocity in every degree of freedom. For conventional submarines with a main propeller and steering fins, the equations of motion are usually modelled as decoupled in longitudinal, lateral, and angular motion (Fossen, 1994). For the control of *Snookie* a similar approximation is used. Each degree of freedom is treated independently, since by design the state of motion for basic operation can be reduced to a much lower number of degrees of freedom. The decoupling of the degrees of freedom is achieved simply by restricting the motion and by adding passive stabilising forces due to the lift of the fins and to shift the centre of body mass below the centre of buoyancy.

Snookie is supposed to always maintain a horizontal orientation, which means that pitch and roll and the respective angular velocities are small. A change in depth is supposed to happen in pure vertical motion. *Snookie* shall move mainly forward. The yaw angle during forward motion is kept small except for turns in place.

The centre of mass $\boldsymbol{\rho}_M$ is shifted below the centre of buoyancy. A deflection in roll angle ϕ leads to a restoring force and a slowly damped oscillation about ϕ_0. This oscillation must be damped by a proportional–derivative (PD) controller in $\dot{\phi}$. The lowered centre of mass also leads to a self-stabilisation with a small stability margin about the pitch angle θ. Pitch θ and yaw ψ are stabilised by the fins counteracting Munk's moment – see Sec. 3.2.7 – to reduce thrust forces necessary to maintain the orientation with the PD controllers. The angular velocity $\boldsymbol{\omega}$ is implicitly given by the derivative part of the PD controllers for θ and ψ.

At pure forward motion the robot is self-stabilising in the horizontal plane aiding the desired horizontal orientation. The shift of the centre of mass below the geometric centre would lead to a roll motion induced for an acceleration $a_y \neq 0$ in y direction and a change in pitch for $a_x \neq 0$, which is counteracted by the fins, as described in Sec. 3.2.7. With the robot being kept horizontal, a_z is decoupled for $\phi \approx 0$ and $\theta \approx 0$, as depth change happens solely through vertical motion. Depth control is achieved by a proportional–derivative (PD) controller in z. Finally, forward velocity v_x is controlled by a proportional–integral (PI) controller to counteract a steady-state error.

The control of decoupled linearised equations of motion with a helicopter-like thruster layout has been previously demonstrated in AMOUR V (Vasilescu et al, 2010). Currently, more sophisticated control methods are investigated to account for the nonlinear dynamics.

4 Flow Sensing in Water

As described in Sec. 2 several groups have already used different types of sensor concepts to realise an ALL. At present none of the sensors is commercially available yet. Flow sensors available on the market, which would promise acceptable accuracy and stability, can hardly be integrated to an ALL and mounted on a robot. For the ALL of *Snookie* a very conservative design decision was made in favour of hot thermistor velocimetry for several reasons.

There is plenty of theory and experience with a very similar sensor concept, the hot wire. Hot wires were shown to in principle provide the necessary accuracy and temporal resolution (Coombs et al, 1989; Franosch et al, 2010). The electronics and the sensors are relatively easy to develop and fabricate. The energy dissipation of the smallest commercially available thermistors allows high integration densities and low energy consumption. A thermistor promises a better signal to noise ratio for small relative signal changes due to its steeper resistance curve compared to a hot wire. And finally, a small thermistor can be embedded in solid material providing the robustness necessary for operation on a moving robot.

4.1 Physics of Hot Thermistor Velocimetry

The temperature of the heated element is given by $T = T_\infty + T_\theta$ with T_∞ being the ambient temperature of the fluid and T_θ the over-temperature. The heat dissipation in a fluid from a small element $P \approx (A + Bv^n) T_\theta$ is a function of the fluid's relative velocity v, where $n \approx 0.5$ and the constants A and B depend on the geometry and the properties of fluid (Middlebrook and Piret, 1950; Felix, 1962; Strickert, 1974; Emsmann and Lehmann, 1975; Perry, 1982; Itsweire and Helland, 1983; Lomas, 1986; Eser, 1990; Bruun, 1996). For a sphere with diameter d (Emsmann and Lehmann, 1975; Eser, 1990) the dissipated power can be approximated by

$$P = \left[2 + 0.55 \left(\frac{\nu c_p \rho}{k} \right)^{0.33} \left(\frac{vd}{\nu} \right)^{0.5} \right] 4\pi \left(\frac{d}{2} \right)^2 \frac{k}{d} T_\theta \tag{31}$$

with specific heat capacity c_p, heat conductivity k, and kinematic viscosity ν. Constant temperature anemometer sense the velocity of a fluid or gas by measuring the power P necessary to keep a heated element at an over-temperature T_θ.

4.2 The Artificial Lateral-Line System of Snookie

Glass-coated thermistors with a diameter of $0.36\,\mathrm{mm}$ from the Honeywell 111 series are used as heated elements for the artificial lateral-line sensors of Snookie. Thermistors are semiconductors with a non-linear negative dependency of electrical resistance upon the temperature. The resistance $R_\vartheta \approx 240\,\Omega$ of a thermistor at working temperature $T \approx 80°\,\mathrm{C}$ with an over-temperature T_θ of approximately $60°\,\mathrm{C}$ is

$$R_\vartheta = R_0 e^{\beta_\vartheta (1/T_0 - 1/T)} \, , \tag{32}$$

given the resistance $1400\,\Omega < R_0 < 2.4\,\mathrm{k\Omega}$ at room temperature T_0 and the constant $2000\,°\mathrm{K} < \beta_\vartheta < 5000\,°\mathrm{K}$. To sustain a constant thermistor temperature the supplied electrical power $P = P_{el} = UI = U^2/R_\vartheta$ must equal the dissipated energy, if all energy is converted to heat and no leakage currents, e.g., due to deficient isolation appear.

The following rough estimates show that it is entirely legitimate to treat the thermistor adiabatically in the sense that it immediately adapts its temperature and thereby its resistance to changes in the transport of heat from it as it has been implicitly assumed in the thermistor model. The voltage necessary to maintain a stable resistance about $240\,\Omega$ of the thermistor in water at rest is approximately $1.5\,\mathrm{V}$, though the properties of the individual sensors are scattered. This results in a dissipated power of approximately $9\,\mathrm{mW}$. For comparison, the total heat stored in a sphere of the size of the thermistor with over-temperature $60°\,\mathrm{C}$ made of silicon or glass is only less than a factor of three larger than the heat dissipated per second. Within a temperature range of $60°$ the thermistor changes its resistance by approximately a factor of five. A change of heat transport due to changing flow conditions must be therefore immediately compensated by a change in the voltage supplied to the thermistor to hold a constant temperature. The voltage

$$U^2 \approx R_\vartheta (A + Bv^n) T_\theta \tag{33}$$

over the sensor is therefore an adiabatic measure for the fluid velocity.

The voltage to keep the thermistor at a constant resistance – and thus at constant temperature – is provided by specially designed boards, which incorporate a Wheatstone bridge and a two-stage amplifier. For easy mounting and maintenance in the snout of Snookie, the thermistor is embedded in a bullet shaped packaging – see Fig. 4. The thermistor is placed at the tip of the bullet.
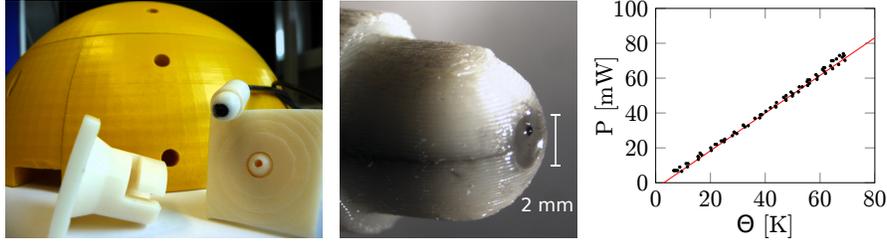
Fig. 4: *Left*: Hull integration. *Middle*: Close-up view of the artificial lateral-line sensor. *Right:* Power dissipated by a thermistor ($R_0 = 1523\,\Omega$ at $T_0 \approx 293\,\mathrm{K}$, mounted on a PCB board and coated) in water vs. over-temperature T_θ. *Black dots*: Measurement of dissipated power P. *Red line*: Linear fit. The relation between energy dissipation and over-temperature is perfectly linear ($1.8\,\mathrm{mW/K}$) as predicted by theory.

4.3 Flow Sensor Calibration

The measured power dissipation of a thermistor (Franosch et al, 2010) confirmed the power law (33) with $n = 0.34$, $A = 1.03\,\mathrm{mW/K}$, and $B = 0.74\,\mathrm{mW/[K(m/s)^n]}$ – see Fig. 4. The actual sensor calibration was done with a tow car. A linear axis (thrusttube, motor 2504 from Copley Controls, encoder resolution $1\,\mu\mathrm{m}$) pulled the sensor through an aquarium of length $1\,\mathrm{m}$ and $0.5\,\mathrm{m}$ in width and height. With constant acceleration from rest all velocities from 0 to $10\,\mathrm{cm/s}$ were present in one measurement. The flow velocity at the tip of the sensors was approximately given by the velocity of the linear axis. The voltage applied to the sensors was sampled with $10\,\mathrm{kHz}$ and filtered with a digital low-pass filter with a cut-off frequency of $5\,\mathrm{Hz}$, since higher frequencies are generally not expected to occur in the hydrodynamic image of stationary objects. The filtered thermistor voltage at given velocity v_A of the linear axis was least-square fitted with

$$v_A = \sqrt[n]{\widetilde{A}U^2 + \widetilde{B}}\,, \tag{34}$$

which can be easily derived from (33) with the substitutions $\widetilde{A} = RA(T - T_0)$ and $\widetilde{B} = RB(T - T_0)$, to obtain $\widetilde{A}$, $\widetilde{B}$ and n.

Figure 5 shows a sensor calibration run. For $v_A > 0.7\,\mathrm{cm/s}$ the shape of the curve resembles very strongly the model described by (34). But for $v_A < 0.7\,\mathrm{cm/s}$ essentially no change in the sensor readings could be observed. This effect was present at all the sensors and calibration runs conducted. Additional complications arise from the fact that the parameters of the model (34) vary not only strongly between the sensors, but also for one sensor in different trials. It was found that this is partially caused by air bubbles generated by the sensors, which locally heat up the water. Gasses dissolved
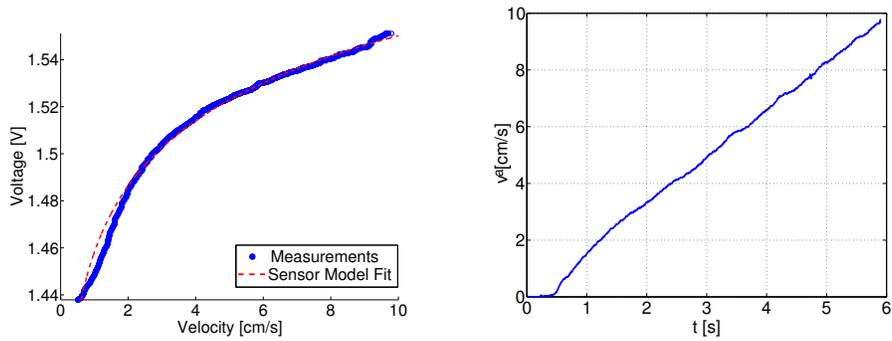
Fig. 5: *Left*: Sensor voltages plotted against velocity of the linear axis. *Right*: Time course of the linear axis velocity of an exemplary calibration run.

in water and released due to heating form small bubbles and cling to the surface of the thermistor. The bubbles partly isolate the sensor. This results in a drift of the initial sensor offset and also in a decreased sensitivity. After removal of the bubbles, the sensor behaviour returns to its initial state, but the generation of the bubbles continues.

The motion of the sensors always started from a longer period at rest with the sensors heating up the surrounding fluid and probably slowly driving thermal convection. As the sensors move away from their resting position at the beginning of the experiment, presumably a transition to the operating regime as described by the theory (34) takes place. It is planned to investigate the reason for the lower bound of velocity by a change of the settings of the experiments. Above $10\,\mathrm{cm/s}$ signals from the sensors quite often become ambiguous which probably attributes to instabilities in the flow over the tip of the sensor.

4.4 Object Detection

For object detection experiments the sensors are placed on a test sphere with a diameter of $15\,\mathrm{cm}$ and 15 sensor mountings as shown in Fig. 6(b), which resembles the snout of Snookie. Of the 15 available slots, 7 are occupied with sensors as indicated in Fig. 6(c). The linear axis is accelerated up to the velocity $v_A = 0.05\,\mathrm{m/s}$. This velocity is then kept constant till the end of the linear axis is reached. For the analysis only the constant velocity part is considered, which can be easily compared to a fluid-dynamics simulation of the experiment. A description of the simulation method can be found in Sec. 5.2.

An obstacle with rectangular cross-section and rounded edges is placed in the aquarium. The whole scenario is depicted in Fig. 6(a). At the closest

distance between sphere and obstacle, the sensor is $3\,\mathrm{mm}$ away from the obstacle. Figure 6 shows the result of the experiment. The simulated velocity at the sensor with the obstacle present is shown for each sensor in the upper plot. The lower plots display the actual measured sensor voltages of both, the experimental run with and without the obstacle for comparison.

The quantitative conclusions that can be drawn from this experiment are limited in a number of ways. The circumstances in the laboratory available at the time the experiments were carried out allowed only a very limited volume of water. Water waves caused by the motion of the spherical mounting and vibrations of the floor contaminated the measurements. The BEM simulation only considered the presence of the spherical mounting and the obstacle and not the walls and the free surface of the aquarium. For an accurate analysis the distance of the walls of the aquarium and the free surface to the obstacle and the sphere should be at least 5 to 10 times the diameter of the sphere. The simulation was reduced to 2D, which is obviously not possible given the experimental situation. The large deviations between simulation and experiment shown in Fig. 6(f) demonstrate such effects. The sensors, in particular the formation of a gas bubbles, were not accurately monitored. An initial state with the fluid at rest in the small aquarium could not be guaranteed given conditions in the laboratory. In any case, our experiments show that the sensors are mechanically and electronically stable over months and that the sensors deliver signals as expected by theory (34) in the range from $7\,\mathrm{mm/s}$ to $10\,\mathrm{cm/s}$. Most importantly the hydrodynamic image of the obstacle shows up in the sensory data. By improving the experimental situation and a careful calibration, acceptable signal to noise ratios suitable for the arrangement of the sensors to an useful artificial lateral line can be expected.

5 Flow-Field Reconstruction

Once the flow velocities measured by the ALL are available for further analysis, the question arises how to proceed.

Simple approximative fluid-mechanical considerations like the investigation of the flow field of a sphere approaching a solid wall (Franosch et al, 2010) by means of the mirror charge method inspire simple heuristics to conclude to the presence of a solid object in close neighbourhood of the ALL. The presence of a solid object would for example increase the mean flow velocity measured by a subset of the sensors. If the object was placed asymmetrically with respect to the longitudinal axis of the robot, it would slightly shift the stagnation point at the stern in dependence of its relative position. By storing the flow patterns of a set of known objects (Fernandez et al, 2007, 2009, 2011) and comparing these flow patterns (templates) with the actual flow velocities, shape and distance of a known object could be identified. But, those heuristics somewhat look at side effects or particular aspects of the hydrodynamic

(a) Sketch of the experiment.

(b) Test sphere.

(c) Schematic of sensor placement.

(d) Sensor 5
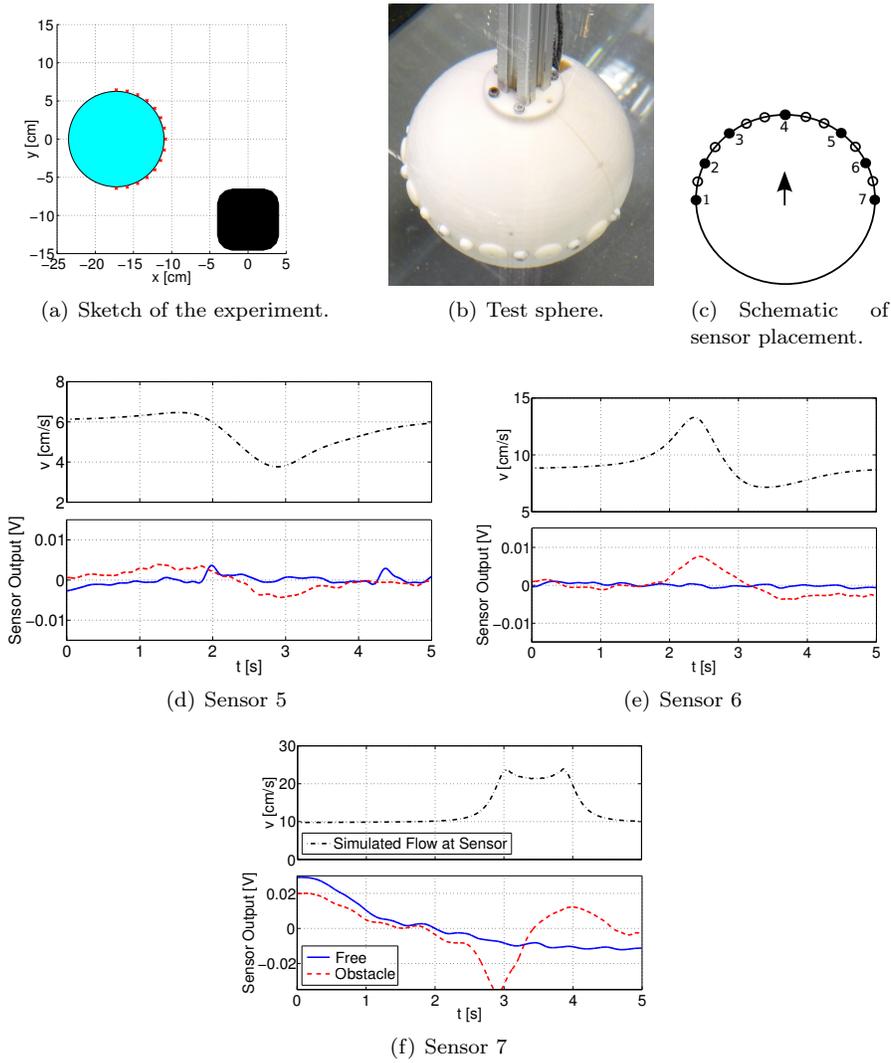

(e) Sensor 6

(f) Sensor 7

Fig. 6: An obstacle detection experiment with simulated flow velocity at the sensors and actual measurements. (a) Schematic of obstacle in relation to test sphere at the beginning of the experiment. (b) Submerged sphere. (c) Schematic of sphere with sensor distribution. Positions with filled circles contain a sensor. (d), (e), (f) Simulated flow velocity at the sensor (*upper plot*) and actual measurements (*lower plot*). The measurements were carried out with and without obstacle for comparison. The mean of each measurement was subtracted to allow a better comparison between the runs. For an explanation of the large deviations between simulation and experiment see Sec. 4.4

mapping of the environment onto the flow sensory system. Accordingly, these heuristics are not universally applicable and will suffer from ambiguities. The question then is first, if it is possible to formulate the hydrodynamic mapping in an as general as possible way so that its properties can be analysed, and second, what this mapping tells about the environment without application of prior knowledge or strong assumptions.

The most universal solution to the problem of extracting information from the hydrodynamic image would then be the inversion of the mapping. To the knowledge of the authors not much has been published yet on inverse problems in fluid-mechanics (Derou et al, 1995; Murray and Ukeiley, 2003; Suzuki and Colonius, 2003). In the following the inversion of a 2D hydrodynamic image is carried out from the flow velocities measured on a circle and on a fish-like shape given incompressible inviscid and irrotational flow. In a real fluid, these conditions are found around the front of the blind Mexican cave fish or *Snookie*, where the lateral line or the ALL is placed, moving through a fluid at rest. The vorticity produced at the surface of the moving body is convected to the rear with the incident flow. This is usually expressed by a high Reynolds number in front of the moving observer, resulting in a inviscid and irrotational flow well described by a velocity potential Φ for the incompressible Euler equations (Lamb, 1945; Panton, 2005).

The fluid domain shall be bounded by stationary solid walls of arbitrary geometry and number.

5.1 Properties of the Hydrodynamic Image

For the sake of simplicity the following analysis is restricted to two spatial dimensions. The body is supposed to move with velocity $\boldsymbol{U}$. As already mentioned in Sec. 3.2.3, for the aforementioned conditions the flow field around the front of the moving body is well described by a velocity potential $\boldsymbol{V} = \nabla \Phi(x, y)$ that suffices the Laplace Equation

$$\Delta \Phi = 0 \tag{35}$$

on the fluid domain $\mathcal{D}$. The domain is bounded by the surface of the moving body $\mathcal{S}$ and eventually by other stationary solid walls with surfaces $\mathcal{W}$. Again, the conventions of Sec. 3.2.1 are used to distinguish between quantities in the FOR and in the BFS. The closed surface of the moving body is composed of the disjoint surfaces $\mathcal{S}_S$, on which the flow sensory system measures the tangential flow velocity $v_\parallel = \partial \Phi / \partial \boldsymbol{t}$ with tangent $\boldsymbol{t}$ of the surface, and the rest of the body S_B where nothing except the no-penetration condition $v_\perp = \partial \Phi / \partial \boldsymbol{n} = 0$ with surface normal $\boldsymbol{n}$ is known about the flow field. Of course, the no-penetration condition is also given on the surface S_S of the sensory system.

The tangential velocity $v_\parallel$ measured by the lateral line may be integrated to obtain the potential $\Phi|_{\mathcal{S}_S}$ on the lateral-line system up to an irrelevant constant. Then, together with the Neumann boundary condition given by the no-penetration condition on the surface $\mathcal{S}_S$ with mounted flow sensors, Cauchy boundary conditions are obtained.

Expressed in coordinates of the FOR, which requires the knowledge of the velocity $\boldsymbol{U}$, the problem is to determine the reconstructed $\hat{\boldsymbol{\Phi}}$ on $\mathcal{D}$ given

$$\Phi|_{\mathcal{S}_S} \qquad \text{and} \qquad \left.\frac{\partial\Phi}{\partial N}\right|_{\mathcal{S}_S} = \boldsymbol{U}\cdot\boldsymbol{N} \qquad (36)$$

on $\mathcal{S}_S$. The choice of the coordinate system – FOR or BFS – does not affect the reconstruction. The transformation of the reconstructed flow field between the FOR $\hat{\boldsymbol{V}}$ and the BFS $\hat{\boldsymbol{v}}$ is identical to the directives described in Sec. 3.2.1.

The Cauchy-Kowalevski theorem guarantees the existence and uniqueness of the solution of the Cauchy problem in some neighbourhood of $\mathcal{S}_S$. The solution of the potential problem (35) is a harmonic and analytic function on $\mathcal{D}$. Therefore, the analytic continuation of the potential to the whole fluid domain on $\mathcal{D}$ (Courant and Hilbert, 1989, pp 505) and even beyond is possible. Given the exact knowledge of the potential and the normal derivative of the potential on $\mathcal{S}_S$, the reconstruction of the potential on $\mathcal{D}$ exists and it is unique. But, similar to many other inverse problems, the problem is ill-posed in the sense that any small error in determining the boundary values on $\mathcal{S}_S$ is amplified exponentially with the distance to $\mathcal{S}_S$ (Hadamard, 1902; Isakov, 1998) and therefore needs regularisation.

In summary, the inversion of the hydrodynamic image exist and is unique, but ill-posed.

A polar coordinate system is the most suitable system for the problem raised in 2D as it is closest to the geometry of horizontal branch of the ALL mounted on the spherical snout of *Snookie*. The flow-field reconstruction is extensible to further 2D geometries by the application of conformal mapping – see Sec. 5.4. The general solution of Laplace's equation is known and must be adapted to the boundary conditions on the sensory system $\mathcal{S}_S$ to obtain the reconstructed flow field $\hat{\boldsymbol{V}}$ on $\mathcal{D}$.

5.2 Boundary-Element Method

Before the solution of the inverse problem is presented, the computation of the forward problem, i.e., the hydrodynamic image on the lateral-line system, is described. The solution of the potential flow on $\mathcal{D}$ can be expressed as surface integral over a distribution of monopole and/or dipole sources of a priori unknown strength distributed over $\mathcal{S}_S$, $\mathcal{S}_B$ and $\mathcal{W}$ (Liu, 2009). In a simple version of the so called boundary element method (BEM) – as implemented

here – pure monopole line sources with constant strength over the line segment are assigned to each element of the discretised boundary. The strengths are determined such that the boundary conditions on all boundary elements are fulfilled. To be precise, to avoid further complications due to the computation of singular integrals and to precisely fulfill the boundary conditions, the monopole line sources were placed on a second surface in the interior of the solid bodies at close distance to the actual surface. This construction does not affect the validity of the solution (Lamb, 1945). The resulting linear system of equations for the monopole strengths was solved directly. Then the flow field was evaluated at any point on $\mathcal{D}$ by the resulting surface integral over the boundary elements and monopoles.

This method has several advantages. It does not require a mesh of the fluid domain, just the boundaries need to be meshed. Independent meshes can simply be moved against each other. The quality of the simulation can be easily assessed by checking the boundary conditions. A major disadvantage is its limitation to potential flow. In a simple version as used here the BEM suffers from high memory consumption.

5.3 The Inversion of the Hydrodynamic Image

The origin of a polar coordinate system (r, ϕ) shall be placed in the centre of the circular flow sensory system with radius r_0 – see Fig. 7. The surface of the moving circle is a streamline and the flow velocity component normal to the circle is zero. Then, the Laplace equation (35) on $\mathcal{D}$ is solved by the Ansatz

$$\Phi(r, \phi) = \sum_\alpha \left(A_\alpha \frac{r^\alpha}{r_0^{\alpha-1}} + B_\alpha \frac{r^{-\alpha}}{r_0^{-\alpha-1}} \right) \mathrm{e}^{i\,\alpha\,\phi} , \tag{37}$$

and $i = \sqrt{-1}$. In the BFS the no-penetration condition (36) on the surface of the moving circle requires $A_\alpha = B_\alpha$, and the radial $\hat{v}_r$ and angular $\hat{v}_\phi$ velocities of the flow field on D are given by

$$\hat{v}_r(r, \phi) = \frac{\partial \Phi}{\partial r} = \sum_\alpha A_\alpha \alpha \left[\left(\frac{r}{r_0} \right)^{\alpha-1} - \left(\frac{r}{r_0} \right)^{-\alpha-1} \right] \mathrm{e}^{i\,\alpha\,\phi} \tag{38a}$$

$$\hat{v}_\phi(r, \phi) = \frac{1}{r} \frac{\partial \Phi}{\partial \phi} = i \sum_\alpha A_\alpha \alpha \left[\left(\frac{r}{r_0} \right)^{\alpha-1} + \left(\frac{r}{r_0} \right)^{-\alpha-1} \right] \mathrm{e}^{i\,\alpha\,\phi} . \tag{38b}$$

The coefficients A_α have to be determined from the measured tangential velocities

$$v_\parallel(r_0, \phi) = 2i \sum_\alpha \alpha A_\alpha \mathrm{e}^{i\,\alpha\,\phi} \tag{39}$$

on the surface of the circle by the Fourier transform,

$$A_a = \frac{1}{4\pi i\alpha} \int_0^{2\pi} v_\parallel(r_0, \phi) \, \mathrm{e}^{-i\alpha\phi} \, \mathrm{d}\phi \, . \tag{40}$$

Figure 7 shows the flow field around a circle moving towards a wall under an angle of 20°. For a finite number of flow sensors the Fourier coefficients are computed by a Fourier series. The frequency regularisation is implicitly carried out by the finite number of sensors considered to obtain A_α by (40).
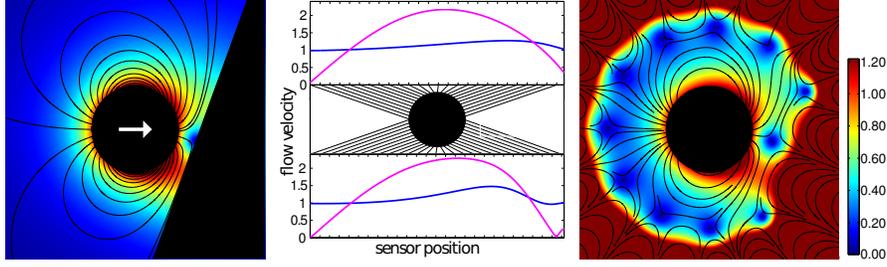

Fig. 7: Reconstruction of the flow field around a circle. The flow velocity is colour coded in units of the speed of the sphere, lengths are scaled by the size of the sphere. *Left*: A circle with 1000 sensors equally distributed on its surface moves towards a wall at a 20° angle. The flow field is plotted with respect to the FOR. *Middle*: The tangential velocities on the surface of the circle are used to determine the coefficients A_α. The measured flow velocities are shown in the BFS (pink line) and the FOR (blue line). The middle part illustrates the unrolling of the surface of the circle onto the x axis of the velocity plot. *Right*: In the reconstructed flow field the wall can be deduced from the parallel streamlines in front of the circle.

5.4 Flow-Field Reconstruction from a Fish-Like Shape

While the circular shape is directly applicable to the artificial lateral system of *Snookie*, the Joukowski transformation allows to apply the reconstruction to the inspiring role model, the blind Mexican cave fish. In the complex plane $z = x + iy$ the circle and the surrounding flow field can be transformed into a fish-like shape and the corresponding flow field by application of a Joukowski transformation (Hassan, 1985)

$$Z(z) = z + \frac{c^2}{z + s} + s \tag{41}$$

with the shape parameters c and s of the resulting aerofoil by the following procedure: measure the velocities on surface of fish; apply the inverse of the

Joukowski transformation (41) to obtain the corresponding flow velocities on surface of the unit circle; reconstruct the flow field around the circle using eqs. (40) and (38); finally, apply the Joukowski transformation (41) on the reconstructed flow field to obtain the flow field around fish – see Fig. 8.

6 Discussion and Outlook

As soon as speed and shape of surrounding objects are available, the lateral line can contribute to more complex tasks involving more than just the detection of the pure presence and classification of an object. For the biological counterparts, some behavioural experiments about map formation of the environment and self localisation with the lateral-line system are already available (Teyke, 1985; Burt de Perera, 2004; Sharma et al, 2009; Patton et al, 2010). Using a lateral-line sensor processing technique as the one described in the previous sections, similar capabilities can be implemented on *Snookie*. *Snookie* is equipped with an inertia sensor system – see Sec. 3.1 – enabling the robot to estimate the current acceleration and by integration the current speed and the relative position. One challenge is that the quality of a map generated during motion depends on the accuracy of the position estimate, which is subject to drift. To counteract this drift, usually external references such as GPS are used, which is highly attenuated underwater. A method without external signals is called simultaneous localisation and mapping (SLAM) (Thrun et al, 2005), building up a map on the fly, which can then be used for matches to verify a position. A method to extract walls from the reconstructed flow field and a theoretical study of SLAM with inertial data and the extracted walls will be published somewhere else (Lenz et al, 2013). Although the reconstruction of the environment around the robot as described in section 5.3 is, due to its mathematical nature, restricted to a close range, the additional matching of the reconstructed wall against the existing continuously refined map allows to compensate for the drifts of the inertial sensory system.

However, for a widely applicable flow sensory system useful in arbitrary environmental condition, several problems have to be solved. First, the reconstruction due to the nature of the problem is very sensitive against small errors in the flow velocity measurement. Any small disturbance increases exponentially with the distance to the sensory system. Therefore, the flow reconstruction requires strong regularisation. The easiest regularisation one can perform is frequency regularisation, as it was carried out for Fig. 7 and 8 by a finite number of sensors used to compute the Fourier Series of the flow velocity on the surface of the sensory system. Simply by omitting the higher spatial frequencies from the Fourier-transform of the measured velocities along the flow sensory system (40), the reconstruction is stabilised for the prize of resolving less details. A follow-up publication with a Thikonov-
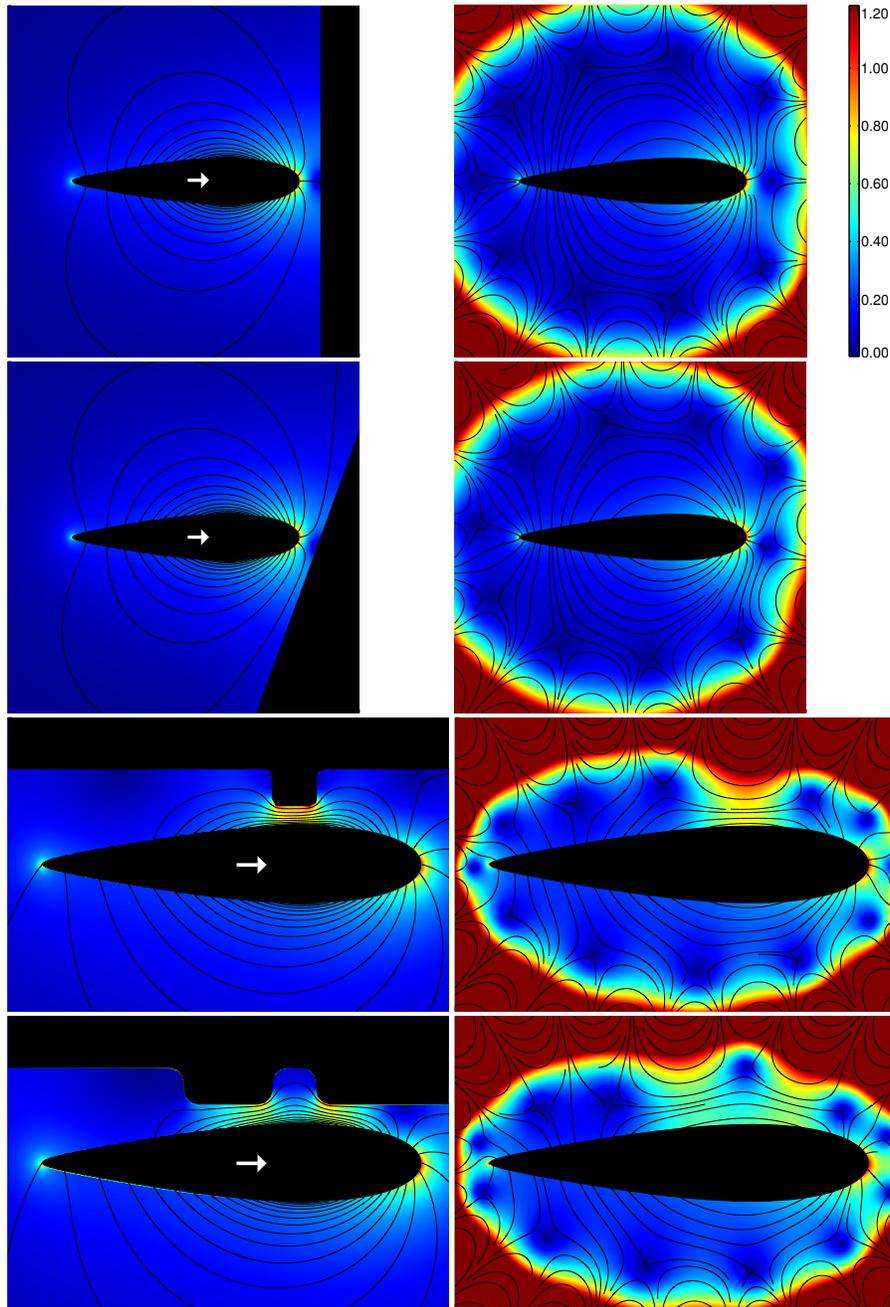
Fig. 8: *Left column:* Flow field and streamlines around a fish. Black: Solid objects and walls, respectively, in the vicinity of the moving fish. The flow velocity is colour coded in units of the speed of the fish, lengths are scaled by the size of the fish. *Right column:* Reconstructed flow field and streamlines in the FOR. The fish can deduce the shape of the wall from the streamlines. The lateral-line organ, which samples the flow field on the surface of the fish, was modelled by 1000 equally spaced sensors.

regularised flow-field reconstruction (TFR) that allows to regularise in dependence of the distance to the sensory system, is in preparation (Urban et al, 2013). While frequency regularisation cuts the fine details globally, the TFR preserves details at least at small distances.

The next step towards a real-world application is to formulate the reconstruction for potential flow in three spatial dimensions. While this seems to be easily doable since it is quite clear how to proceed mathematically, the step towards more realistic flow conditions with vorticity might be challenging.

Fish are certainly interested in the fluid motion surrounding them for wake tracking or improved motion control. The fluid may be also considered as the medium through which boundaries and the motion of boundaries are mapped onto the lateral-line system. It is possible to extract the boundaries (Lenz et al, 2013) from the reconstructed flow field. However, one could also think of methods to directly conclude to the shape and location of boundaries given the hydrodynamic image on the sensory system without preceding reconstruction of the flow field.

From the more practical side, the next steps in realising an ALL that can actually be mounted on a swimming robot are improvements in calibration and the experimental test conditions. For a convincing comparison with simulations a 3D BEM is desirable. For the reliable and enduring operation on an autonomous underwater robot the formation of bubbles on the thermistor remains an issue to be solved. Experiments with hydrophilic coatings so far did not lead to convincing results. It has already been shown experimentally by several groups that in principle detection (Martiny et al, 2009; Yang et al, 2011) and classification (Fernandez et al, 2011) based on an artificial lateral with different sensor concepts is possible. The flow-field reconstruction requires an albeit small but carefully calibrated set of flow sensors.

The discussion of the dynamics of the robot shows that additional forces appear in the close vicinity of boundaries such as a free surface or solid walls. The control of the thrusters, the correct treatment and computation of the added masses, and incorporating corrections to the added masses in the presence of a wall offer large space for the improvements of the dynamics of a highly manoeuvrable robot. This also requires extending the design of the hardware, e.g. a separate controller for each thruster surveying rotation speed of the propeller and electric current. Of course, the flow-field reconstruction by the ALL may also be used to improve the dynamical model used for control online during operation.

7 Acronyms

2D	2-dimensional
3D	3-dimensional
6D	6-dimensional
ALL	artificial lateral-line system
AUV	autonomous underwater vehicle
BCCN	Bernstein Center for Computational Neuroscience
BEM	boundary-element method
BFS	*body-fixed system*
CAD	computer aided design
CoTeSys	Cognition for Technical Systems
FOR	*frame of reference*
MEMS	micro-electro-mechanical systems
PD	proportional–derivative
PI	proportional–integral
PVDF	polyvinylidene fluoride fibers
PWM	pulse-width modulation
ROS	Robot Operating System
SLAM	simultaneous localisation and mapping
TFR	Thikonov-regularised flow-field reconstruction

Akanyeti O, Venturelli R, Visentin F, Chambers L, Megill WM, Fiorini P (2011) What information do Kármán streets offer to flow sensing? Bioinspiration & Biomimetics 6(3):036,001

Bleckmann H (2008) Peripheral and central processing of lateral line information. Journal of Comparative Physiology A 194(2):145–158

Bleckmann H, Zelick R (2009) Lateral line system of fish. Integrative Zoology 4(1):13–25

Bleckmann H, Breithaupt T, Blickhan R, Tautz J (1991) The time course and frequency content of hydrodynamic events caused by moving fish, frogs, and *Crustaceans*. Journal of Comparative Physiology A 168(6)

Bouffanais R, Weymouth GD, Yue DKP (2010) Hydrodynamic object recognition using pressure sensing. Proceedings of the Royal Society A: Mathematical, Physical and Engineering Sciences 467(2125):19–38

Brennen CE (1982) A review of added mass and fluid inertial forces. Tech. rep.

Breslin JP, Andersen P (2008) Hydrodynamics of Ship Propellers. Cambridge University Press

Bruun HH (1996) Hot wire anemometry. Oxford Univ. Press, Oxford

Burt de Perera T (2004) Spatial parameters encoded in the spatial map of the blind Mexican cave fish, *Astyanax fasciatus*. Animal Behaviour 68(2):291–295

von Campenhausen C, Riess I, Weissert R (1981) Detection of stationary objects by the blind cave fish *Anoptichthys jordani* (*Characidae*). Journal of Comparative Physiology A 143:369–374

Chagnaud BP, Bleckmann H, Engelmann J (2006) Neural responses of goldfish lateral line afferents to vortex motions. The Journal of Experimental Biology 209(2):327–42

Chen J, Engel J, Chen N, Pandya SD, Coombs S, Liu C (2006) Artificial lateral line and hydrodynamic object tracking. In: 19th IEEE International Conference on Micro Electro Mechanical Systems, IEEE, pp 694–697

Conley RA, Coombs S (1998) Dipole source localization by mottled sculpin III. orientation after site-specific, unilateral denervation of the lateral line system. Journal of Comparative Physiology A 183(3):335–344

Coombs S (1994) Nearfield detection of dipole sources by the goldfish (*Carassius auratus*) and the mottled sculpin (*Cottus bairdi*). The Journal of Experimental Biology 190(1):109–129

Coombs S, Conley RA (1997a) Dipole source localization by mottled sculpin I. approach strategies. Journal of Comparative Physiology A 180(4):387–399

Coombs S, Conley RA (1997b) Dipole source localization by the mottled sculpin II. the role of lateral line excitation patterns. Journal of Comparative Physiology A 180(4):401–415

Coombs S, van Netten SM (2005) The hydrodynamics and structural mechanics of the lateral line system. Fish Physiology 23:103–139

Coombs S, Patton P (2009) Lateral line stimulation patterns and prey orienting behavior in the Lake Michigan mottled sculpin (*Cottus bairdi*). Journal of Comparative Physiology A 195(3):279–97

Coombs S, Fay RR, Janssen J (1989) Hot-film anemometry for measuring lateral line stimuli. The Journal of the Acoustical Society of America 85(5):2185–2193

Coombs S, Hastings M, Finneran J (1996) Modeling and measuring lateral line excitation patterns to changing dipole source locations. Journal of Comparative Physiology A 178(3)

Coombs S, Braun CB, Donovan B (2001) The orienting response of Lake Michigan mottled sculpin is mediated by canal neuromasts. The Journal of Experimental Biology 204(2):337–348

Courant R, Hilbert D (1989) Methods of Mathematical Physics, vol 1. Wiley-VCH

Curcić-Blake B, van Netten SM (2005) Rapid responses of the cupula in the lateral line of ruffe (*Gymnocephalus cernuus*). Journal of Comparative Physiology A 191(4):393–401

Curcić-Blake B, van Netten SM (2006) Source location encoding in the fish lateral line canal. The Journal of Experimental Biology 209(8):1548–59

Dagamseh A, Wiegerink R, Lammerink T, Krijnen G (2013) Imaging dipole flow sources using an artificial lateral-line system made of biomimetic hair flow sensors. Interface 10(83):20130,162

Dehnhardt G, Mauck B, Hanke W, Bleckmann H (2001) Hydrodynamic trail-following in harbor seals (*Phoca vitulina*). Science (New York, NY) 293(5527):102–4

Derou D, Dinten J, Herault L, Niez J (1995) Physical-model based reconstruction of the global instantaneous velocity field from velocity measurement at a few points. In: Proceedings of the Workshop on Physics-Based Modeling in Computer Vision, IEEE Comput. Soc. Press, p 63

Dijkgraaf S (1933) Untersuchungen über die Funktion der Seitenorgane an Fischen. Zeitschrift für Vergleichende Physiologie 20(1-2):162–214

Dijkgraaf S (1963) The functioning and significance of the lateral-line organs. Biological Reviews 38(1):51–105

Emsmann S, Lehmann A (1975) Entwicklung eines Thermistoranemometers zur Messung instationärer Wassergeschwindigkeiten. Fortschrittsberichte der VDI Zeitschriften 18(8)

Engelmann J, Bleckmann H (2004) Coding of lateral line stimuli in the goldfish midbrain in still and running water. Zoology 107(2):135–51

Engelmann J, Hanke W, Bleckmann H (2002) Lateral line reception in still- and running water. Journal of Comparative Physiology A 188(7):513–26

Eser U (1990) Thermisches Anemometer mit Kugelsonde zur Bestimmung kleiner Geschwindigkeitsvektoren. PhD thesis, Universität Essen, Essen

Feldman J (1979) DTNSRDC revised standard submarine equations of motion. Tech. rep., DTNSRDC

Felix W (1962) Strömungsmessung mit Thermistoren. Naunyn-Schmiedberg's Arch exp Path u Pharmak 244:254–269

Fernandez VI, Hou SM, Hover F, Lang JH, Triantafyllou M (2007) Lateral-line inspired mems-array pressure sensing for passive underwater navigation. Tech. rep., MIT Sea Grant

Fernandez VI, Hou SM, Hover FS (2009) Development and application of distributed MEMS pressure sensor array for AUV object avoidance. Tech. rep., MIT Sea Grant

Fernandez VI, Maertens A, Yaul FM, Dahl J, Lang JH, Triantafyllou MS (2011) Lateral-line-inspired sensor arrays for navigation and object identification. Marine Technology Society Journal 45(4):130–146

Fossen TI (1994) Guidance and Control of Ocean Vehicles. Wiley

Franosch JM, Hagedorn H, Goulet J, Engelmann J, van Hemmen JL (2009) Wake tracking and the detection of vortex rings by the canal lateral line of fish. Physical Review Letters 103(7)

Franosch JMP, Sichert AB, Suttner MD, van Hemmen JL (2005) Estimating position and velocity of a submerged moving object by the clawed frog *Xenopus* and by fish – a cybernetic approach. Biological Cybernetics 93(4):231–8

Franosch JmP, Sosnowski S, Chami NK, Hirche S (2010) Biomimetic lateral-line system for underwater vehicles. In: 9th IEEE Sensors Conference

Geer J (1975) Uniform asymptotic solutions for potential flow about a slender body of revolution. Journal of Fluid Mechanics 67(04):817–827

Goulet J, Engelmann J, Chagnaud BP, Franosch JMP, Suttner MD, van Hemmen JL (2008) Object localization through the lateral line system of fish: theory and experiment. Journal of Comparative Physiology A 194(1):1–17

Hadamard J (1902) Sur les problèmes aux dérivés partielles et leur signification physique. Princeton University Bulletin 13:49 – 52

Handelsman RA, Keller JB (1967) Axially symmetric potential flow around a slender body. Journal of Fluid Mechanics 28(01):131–147

Hanke W (2004) The hydrodynamic trails of *Lepomis gibbosus* (*Centrarchidae*), *Colomesus psittacus* (*Tetraodontidae*) and *Thysochromis ansorgii* (*Cichlidae*) investigated with scanning particle image velocimetry. Journal of Experimental Biology 207(9):1585–1596

Hanke W, Brucker C, Bleckmann H (2000) The ageing of the low-frequency water disturbances caused by swimming goldfish and its possible relevance to prey detection. The Journal of Experimental Biology 203(7):1193–1200

Hassan ES (1985) Mathematical analysis of the stimulus for the lateral line organ. Biological Cybernetics 52(1):23–36

Hassan ES (1986) On the discrimination of spatial intervals by the blind cave fish (*Anoptichthys jordani*). Journal of Comparative Physiology A 159(5):701–710

Hassan ES (1989) Hydrodynamic imaging of the surroundings by the lateral line of the blind cave fish *Anoptichthys jordani*. In: The Mechanosensory Lateral Line, pp 217–227

Hassan ES (1992a) Mathematical description of the stimuli to the lateral line system of fish derived from a three-dimensional flow field analysis I. The cases of moving in open water and of gliding towards a plane surface. Biological Cybernetics 66(5):453–461

Hassan ES (1992b) Mathematical description of the stimuli to the lateral line system of fish derived from a three-dimensional flow field analysis II. The case of gliding alongside or above a plane surface. Biological Cybernetics 66(5):443–452

Hassan ES (1993) Mathematical description of the stimuli to the lateral line system of fish, derived from a three-dimensional flow field analysis III. The case of an oscillating sphere near the fish. Biological Cybernetics 69(5-6):525–538

Howe MS (2006) Hydrodynamics and Sound. Cambridge University Press

Hsieh TY, Huang SW, Mu LJ, Chen E, Guo J (2011) Artificial lateral line design for robotic fish. In: Underwater Technology (UT), 2011 IEEE Symposium on and 2011 Workshop on Scientific Use of Submarine Cables and Related Technologies (SSC), pp 1–6

Isakov V (1998) Inverse Problems for Partial Differential Equations. Applied Mathematical Sciences, Springer

Itsweire IC, Helland KN (1983) A high-performance low-cost constant-temperature hot-wire anemometer. Journal of Physics E-Scientific Instruments 16(6):549–553

Izadi N, de Boer MJ, Berenschot JW, Krijnen GJM (2010) Fabrication of superficial neuromast inspired capacitive flow sensors. Journal of Micromechanics and Microengineering 20(8):85,041

Kinsey JC, Eustice RM, Whitcomb LL (2006) A survey of underwater vehicle navigation: recent advances and new challanges. In: IFAC Conference of Manoeuvering and Control of Marine Craft, Lisbon, Portugal

Kirchhoff GR (1870) Über die Bewegung eines Rotationskörpers in einer Flüssigkeit. Journal für die reine und angewandte Mathematik (71):237–262

Klein A, Bleckmann H (2011) Determination of object position, vortex shedding frequency and flow velocity using artificial lateral line canals. Beilstein Journal of Nanotechnology 2:276–83

Klein A, Herzog H, Bleckmann H (2011) Lateral line canal morphology and signal to noise ratio. In: SPIE Smart Structures and Materials + Nondestructive Evaluation and Health Monitoring, International Society for Optics and Photonics, pp 797,507–797,507–6

Klein A, Münz H, Bleckmann H (2013) The functional significance of lateral line canal morphology on the trunk of the marine teleost *Xiphister atropurpureus* (*Stichaeidae*). Journal of comparative physiology A 199(9):735–49

Korotkin AI (2010) Added Masses of Ship Structures. Fluid Mechanics and Its Applications, Springer

Kröther S, Mogdans J, Bleckmann H (2002) Brainstem lateral line responses to sinusoidal wave stimuli in still and running water. The Journal of Experimental Biology 205(10):1471–84

Künzel S, Bleckmann H, Mogdans J (2011) Responses of brainstem lateral line units to different stimulus source locations and vibration directions. Journal of Comparative Physiology A 197(7):773–87

Lamb H (1945) Hydrodynamics, 6th edn. Dover publications

Lenz D, Sosnowski S, Vollmayr AN, van Hemmen JL, Hirche S (2013) SLAM with an artificial lateral-line system. **In preparation**

Lewandowski EM (2003) The Dynamics of Marine Craft: Maneuvering and Seakeeping. World Scientific Pub Co Inc

Li F, Liu W, Stefanini C, Fu X, Dario P (2010) A novel bioinspired PVDF micro/nano hair receptor for a robot sensing system. Sensors 10(1):994–1011

Liu C (2007) Micromachined biomimetic artificial haircell sensors. Bioinspiration & Biomimetics 2(4):162–169

Liu Y (2009) Fast Multipole Boundary Element Method: Theory and Applications in Engineering, 1st edn. Cambridge University Press

Lomas CG (1986) Fundamentals of hot wire anemometry. Cambridge University Press, Cambridge

Martiny N, Sosnowski S, Hirche S, Nie Y, Franosch JMP (2009) Design of a lateral-line sensor for an autonomous underwater vehicle. In: 8th IFAC

International Conference on Manoeuvring and Control of Marine Craft, Guaruja, Brazil, pp 292–297

McHenry MJ, Strother JA, van Netten SM (2008) Mechanical filtering by the boundary layer and fluid-structure interaction in the superficial neuromast of the fish lateral line system. Journal of Comparative Physiology A 194(9):795–810

Meirovitch L (2004) Methods of Analytical Dynamics. Dover Civil and Mechanical Engineering, Dover Publications

Meyer G, Klein A, Mogdans J, Bleckmann H (2012) Toral lateral line units of goldfish, *Carassius auratus*, are sensitive to the position and vibration direction of a vibrating sphere. Journal of Comparative Physiology A

Middlebrook GB, Piret EL (1950) Hot wire anemometry-solution of some difficulties in measurement of low water velocities. Industrial and Engineering Chemistry 42(8)

Mogdans J, Bleckmann H (2012) Coping with flow: behavior, neurophysiology and modeling of the fish lateral line system. Biological Cybernetics 106(11-12):627–42

Motamed M, Yan J (2005) A review of biological, biomimetic and miniature force sensing for microflight. 2005 IEEERSJ International Conference on Intelligent Robots and Systems pp 2630–2637

Murray NE, Ukeiley LS (2003) Estimation of the flowfield from surface pressure measurements in an open cavity. AIAA Journal 41(5):969–972

van Netten SM (2006) Hydrodynamic detection by cupulae in a lateral line canal: functional relations between physics and physiology. Biological Cybernetics 94(1):67–85

Newman JN (1977) Marine Hydrodynamics. MIT Press

Nguyen N, Jones DL, Yang Y, Liu C (2011) Flow vision for autonomous underwater vehicles via an artificial lateral line. EURASIP Journal on Advances in Signal Processing 2011(1):806,406

Nicholson JW, Healey AJ (2008) The present state of autonomous underwater vehicle (AUV) applications and technologies. Marine Technology Society Journal 42(1):8

Nie Y, Franosch JMP, van Hemmen JL (2013) How blind fish can detect walls by measuring body deceleration. **In preparation**

Obasaju ED, Bearman PW, Graham JMR (1988) A study of forces, circulation and vortex patterns around a circular cylinder in oscillating flow. Journal of Fluid Mechanics 196(-1):467–494

Oertel H, Mayes K (eds) (2004) Prandtl's Essentials of Fluid Mechanics, 2nd edn. Applied Mathematical Sciences, Springer

Pandya S, Yang Y, Liu C, Jones DL (2007) Biomimetic imaging of flow phenomna. IEEE International Conference on Acoustics, Speech and Signal Processing, 2007 ICASSP 2007 2:933–936

Pandya SD, Yang Y, Jones DL, Engel J, Liu C (2006) Multisensor processing algorithms for underwater dipole localization and tracking using mems

artificial lateral-line sensors. EURASIP Journal on Advances in Signal Processing pp 1–8

Panton R (2005) Incompressible flow, 3rd edn. J. Wiley, New York

Partridge BL, Pitcher TJ (1980) The sensory basis of fish schools: Relative roles of lateral line and vision. Journal of Comparative Physiology A 135(4):315–325

Patton P, Windsor S, Coombs S (2010) Active wall following by Mexican blind cavefish (*Astyanax mexicanus*). Journal of Comparative Physiology A 196(11):853–867

Peleshanko S, Julian MD, Ornatska M, McConney ME, LeMieux MC, Chen N, Tucker C, Yang Y, Liu C, Humphrey JAC, Tsukruk VV (2007) Hydrogel-encapsulated microfabricated haircells mimicking fish cupula neuromast. Advanced Materials 19(19):2903–2909

Perry AE (1982) Hot-wire anemometry. Clarendon Press, Oxford

Plachta DTT (2003) A hydrodynamic topographic map in the midbrain of goldfish *Carassius auratus*. Journal of Experimental Biology 206(19):3479–3486

Pohlmann K, Grasso FW, Breithaupt T (2001) Tracking wakes: the nocturnal predatory strategy of piscivorous catfish. Proceedings of the National Academy of Sciences of the United States of America 98(13):7371–4

Pohlmann K, Atema J, Breithaupt T (2004) The importance of the lateral line in nocturnal predation of piscivorous catfish. The Journal of Experimental Biology 207(17):2971–8

Qualtieri A, Rizzi F, Todaro MT, Passaseo A, Cingolani R, De Vittorio M (2011) Stress-driven AlN cantilever-based flow sensor for fish lateral line system. Microelectron Eng 88(8):2376–2378

Sharma S, Coombs S, Patton P, Burt de Perera T (2009) The function of wall-following behaviors in the Mexican blind cavefish and a sighted relative, the *Mexican tetra* (*Astyanax*). Journal of Comparative Physiology A 195(3):225–40

Sichert A, Bamler R, van Hemmen JL (2009) Hydrodynamic object recognition: When multipoles count. Physical Review Letters 102(5)

Sosnowski S, Franosch JmP, Zhang L, Nie Y, Hirche S (2010) Simulation of the underwater vehicle "Snookie": Navigating like a fish. In: 1st International Conference on Applied Bionics and Biomechanics

Strickert H (1974) Hitzdraht-und Hitzfilmanemometrie. VEB Verlag Technik, Berlin

Suzuki T, Colonius T (2003) Inverse-imaging method for detection of a vortex in a channel. AIAA Journal 41(9):1743–1751

Teyke T (1985) Collision with and avoidance of obstacles by blind cave fish *Anoptichthys jordani* (*Characidae*). Journal of Comparative Physiology A 157(6):837–843

Thrun S, Burgard W, Fox D (2005) Probabilistic Robotics (Intelligent Robotics and Autonomous Agents series). MIT Press

Urban S, Vollmayr AN, Sosnowski S, Hirche S, van Hemmen JL (2013) Hydrodynamic imaging on a 1-dimensional manifold and its inversion in 2-dimensional potential flow. **In preparation**

Van Trump WJ, McHenry MJ (2008) The morphology and mechanical sensitivity of lateral line receptors in zebrafish larvae (*Danio rerio*). The Journal of Experimental Biology 211(13):2105–15

Vasilescu I, Detweiler C, Doniec M, Gurdan D, Sosnowski S, Stumpf J, Rus D (2010) AMOUR V: A hovering energy efficient underwater robot capable of dynamic payloads. The International Journal of Robotics Research OnlineFirst 29:547–570

Vogel D, Bleckmann H (2001) Behavioral discrimination of water motions caused by moving objects 186(12):1107–1117

Weissert R, von Campenhausen C (1981) Discrimination between stationary objects by the blind cave fish *Anoptichthys jordani* (*Characidae*). Journal of Comparative Physiology A 143(3):375–381

Wieskotten S, Mauck B, Miersch L, Dehnhardt G, Hanke W (2011) Hydrodynamic discrimination of wakes caused by objects of different size or shape in a harbour seal (*Phoca vitulina*). The Journal of Experimental Biology 214(11):1922–30

Windsor SP, Tan D, Montgomery JC (2008) Swimming kinematics and hydrodynamic imaging in the blind Mexican cave fish (*Astyanax fasciatus*). Journal of Experimental Biology 211(18):2950–2959

Windsor SP, Norris SE, Cameron SM, Mallinson GD, Montgomery JC (2010a) The flow fields involved in hydrodynamic imaging by blind Mexican cave fish (*Astyanax fasciatus*). Part I: open water and heading towards a wall. Journal of Experimental Biology 213(22):3819–3831

Windsor SP, Norris SE, Cameron SM, Mallinson GD, Montgomery JC (2010b) The flow fields involved in hydrodynamic imaging by blind Mexican cave fish (*Astyanax fasciatus*). Part II: gliding parallel to a wall. Journal of Experimental Biology 213(22):3832–3842

Yang Y, Chen J, Engel J, Pandya S, Chen N, Tucker C, Coombs S, Jones DL, Liu C (2006) Distant touch hydrodynamic imaging with an artificial lateral line. Proceedings of the National Academy of Sciences of the United States of America 103(50):18,891–5

Yang Y, Nguyen N, Chen N, Lockwood M, Tucker C, Hu H, Bleckmann H, Liu C, Jones DL (2010) Artificial lateral line with biomimetic neuromasts to emulate fish sensing. Bioinspiration & Biomimetics 5(1):16,001

Yang Y, Klein A, Bleckmann H, Liu C (2011) Artificial lateral line canal for hydrodynamic detection. Applied Physics Letters 99(2):023,701